Estimating Source Region Influences on Black Carbon Abundance, Microphysics, and Radiative Effect Observed over South Korea

Kara D. Lamb[1,2], Anne E. Perring[1,2,*], Bjørn Samset[3], Dave Peterson[4], Sean Davis[1,2], Bruce E. Anderson[6], Andreas Beyersdorf[6,7], Donald R. Blake[8], Pedro Campuzano-Jost[1,9], Chelsea A. Corr[6], Glenn S. Diskin[6], Yutaka Kondo[10], Nobuhiro Moteki[11], Benjamin A. Nault[1,9], Jun Oh[5,12], Minsu Park[13], Sally E. Pusede[14], Isobel J. Simpson[8], Kenneth L. Thornhill[6], Armin Wisthaler[15,16], and Joshua P. Schwarz[2]

[1]Cooperative Institute for Research in the Environmental Sciences (CIRES), University of Colorado, Boulder, Boulder, CO, USA

[2] NOAA Earth System Research Laboratory (ESRL), Chemical Sciences Division, Boulder, Colorado, USA

[3]University of Oslo, Oslo, Norway

[4]Naval Research Laboratory, Monterey, CA, USA

[5]Department of Air Quality Research, Climate and Air Quality Research Division, National Institute for Environmental Research, Incheon, S. Korea

[6]NASA Langley Research Center, Hampton, VA, USA
[7]California State University, San Bernardino, CA, USA

[8]Department of Chemistry, University of California Irvine, Irvine CA, USA

[9]Department of Chemistry and Biochemistry, University of Colorado, Boulder, Boulder, CO, USA

[10]National Institute of Polar Research, Tachikawa, Japan

[11]Department of Earth and Planetary Science, Graduate School of Science, University of Tokyo, Tokyo, Japan

[12]Department of Environmental Science, Hankuk University of Foreign Studies, S. Korea

[13]Department of Atmospheric Sciences, Yonsei University, Seoul, S. Korea

[14]Department of Environmental Sciences, University of Virginia, Charlottesville, VA, USA

[15]Institute for Ion Physics and Applied Physics, University of Innsbruck, Austria

[16]Department of Chemistry, University of Oslo, Oslo, Norway

*Currently at Department of Chemistry, Colgate University, Hamilton, NY

Corresponding author: Kara Lamb (kara.lamb@noaa.gov)

Key Points:

- Black carbon vertical profiles observed in late spring 2016 in South Korea were consistent with strong regional sources.
- The profiles systematically measured over a single site varied due to meteorologically-driven changes in transport.
- South Korea, China, and Russia were the major source-region contributors to black carbon column direct radiative effect.

Abstract

East Asia is the strongest global source region for anthropogenic black carbon (BC), the most important light-absorbing aerosol contributing to direct radiative climate forcing. To provide extended observational constraints on regional BC distributions and impacts, *in situ* measurements of BC were obtained with a single particle soot photometer during the May/June 2016 KORUS-AQ (Korean-US Air Quality) aircraft campaign in South Korea. Unique chemical tracer relationships were associated with BC sourced from different regions. The extent and variability in vertical BC mass burden for 48 profiles over a single site near Seoul was investigated using back-trajectory and chemical tracer analysis. Meteorologically-driven changes in transport influenced the relative importance of different source regions, impacting observed BC loadings at all altitudes. Internal mixing- and size-distributions of BC further demonstrated dependence on source region: BC attributed to China had a larger mass median diameter (180 ±13 nm) than BC attributed to South Korea (152±25 nm), and BC associated with long range transport was less thickly coated (60±4 nm) than that sourced from South Korea (75±16 nm). The column BC direct radiative effect at the top of the atmosphere was estimated to be $1.0^{+0.9}_{-0.5}$ W/m^2, with average values for different meteorological periods varying by a factor of 2 due to changes in the BC vertical profile. During the campaign, BC sourced from South Korea (≤ 31%), China (22%), and Russia (14%) were the most significant single-region contributors to the column direct radiative effect.

1 Introduction

East Asia is the strongest anthropogenic source region for black carbon (BC), which is emitted during incomplete combustion and is the dominant anthropogenic light-absorbing aerosol (Bond et al., 2013). Although BC has a short atmospheric lifetime of a few days to weeks, it strongly impacts absorption of solar radiation. The direct climate effect is typically expressed as the total effect on the top-of-atmosphere radiation balance, and the global BC direct climate effect was estimated from the AEROCOM (Aerosol Comparisons between Observations and Models) project to be 0.4 (0.05 to 0.8) W/m^2 (Myhre et al., 2013). Regional direct climate effects from BC can be significantly larger near sources and model variability is highest in the strongest source regions, including East Asia (Myhre et al., 2013). While the temperature impact of present-day BC is modest globally, it may be significant regionally (Stjern et al. 2017).

Direct radiative effects from BC depend strongly on its vertically-distributed mass loadings, size distributions, and association with internally mixed materials, all of which vary by source and region (Bond et al., 2013). Internal mixing, which enhances absorption of solar radiation (Jacobson 2001; Cappa et al., 2012; Liu et al., 2017), is dependent on both source and co-emitted species, as well as aging in the atmosphere, as BC becomes increasingly “coated” during transport from condensation of gas phase species (Moteki et al., 2007; Shiraiwa et al., 2007). The vertical distribution of BC is also important, as BC’s forcing efficiency increases dramatically with altitude (Zarzycki & Bond, 2010; Samset & Myhre, 2011). However, the vertical distribution of aerosols is challenging to predict (Samset et al. 2013; Kipling et al., 2016). Three-dimensional model simulations with resolved particle size and mixing state estimated the regional BC direct radiative effect in East Asia as 1.6-2.8 W/m^2 at the top of the atmosphere, for model runs focusing on the spring of 2009 (Matsui 2016a; 2016b), with most variability arising from uncertainty in BC size and mixing state. Given the climatic impacts of BC sourced from

East Asia, additional observational constraints on regional BC vertical profiles and optical properties are needed.

Previous ground-based and aircraft-based measurements in East Asia have demonstrated that internal mixing state, and therefore radiative properties of BC, are dependent on source region and aging timescale since emission. Aircraft measurements of BC, using a Single Particle Soot Photometer (SP2) on research flights near the coast of Japan in March 2004, showed that particles in urban plumes sourced from East Asia became increasingly internally mixed over ~12 hours (Moteki et al., 2007). Similarly, a ground-based study located at an urban site north of Tokyo found that transported, polluted urban air exhibited an increasing number fraction of BC internally mixed with sulfate and organics, with increasing photochemical age (Shiraiwa et al., 2007). Ground-based measurements on Fukue Island, Japan showed that air sourced from continental Asia was more internally mixed than air sourced from Japan or the free troposphere (Shiraiwa et al., 2008). More recent measurements at Noto Peninsula, Japan found significant light absorption enhancement for BC sourced from China (Ueda et al., 2016). A comparison of measurements near an industrial site to those at a remote site on Fukue Island indicated secondary formation of sulfate and organic aerosols led to increases in BC coatings for transported aerosols (Miyakawa et al., 2017).

The size dependence of BC aerosol has been shown to be related to source, atmospheric lifetime, and transport efficiency. BC sourced from biomass burning typically has a larger mass median diameter than BC sourced from urban emissions (Schwarz et al., 2008a). BC transport efficiency has been shown to be inversely correlated with BC size (Moteki et al., 2012), with larger particles removed more efficiently. This transport efficiency was shown to be source-region-dependent for air sampled over the East China Sea from different source regions in China during the A-FORCE 2009 campaign (Oshima et al., 2012). Air masses sampled on Fukue Island in the spring of 2015 that originated in southern China were also shown to be strongly influenced by wet removal (Miyakwa et al., 2017). Observed BC size distributions in East Asia during the A-FORCE 2013W campaign demonstrated an altitude dependence, with typically decreasing size distributions at higher altitudes associated with wet removal (Kondo et al., 2016). This preferential removal of larger BC particles was linked to nucleation scavenging by comparing ground-based measurements of BC in air following rain events to BC removed in rainwater in Tokyo (Ohata et al., 2016b). BC size may impact its mass absorption cross section (MAC), which links the mass concentration of BC to its optical effects, with the largest MAC values associated with mass median diameters <150 nm (Adler et al., 2013; Schwarz et al., 2013a; Moteki et al., 2017).

Asian outflow is known to be a significant source of pollutants to other parts of the world, including North America (Hadley et al., 2007) and the Arctic (Matsui et al., 2011). Observed BC concentrations and altitude-dependence in air transported to the Arctic from East Asia during the spring/summer 2008 ARCTAS campaign were strongly dependent on season and origin of air, with significant differences between biomass burning aerosols sourced from Russia and anthropogenic aerosols from East Asia (Matsui et al., 2011). Measurements over the remote Pacific in 2010-2011 during the HIPPO campaigns indicated that Asian outflow has a strong seasonal dependence, with highest BC loadings in remote regions associated with Asian outflow in the spring (Schwarz et al., 2010a; Schwarz et al., 2013b; Shen et al., 2014). This strong seasonal dependence has been linked to an overestimation of BC loadings in remote regions in global models (Wang et al., 2014a). Long-term monitoring (from 2009-2015) of Asian continental outflow on Fukue Island also found a strong seasonal dependence to transport, with the highest concentrations in the autumn, winter, and spring (Kanaya et al., 2016).

To assess the impact of BC sourced in East Asia on both direct and indirect climate effects, *in situ* measurements of BC loadings, internal mixing state, and size distributions were made over South Korea during the NASA Korean-United States Air Quality Study (KORUS-AQ) in May/June of 2016. An SP2 was flown to provide continuous real-time measurements of refractory black carbon (rBC) on a single particle basis (Petzold et al. 2013), providing both rBC mass loadings and size distributions, as well as information about the presence and amount of materials internally mixed with rBC (Schwarz et al., 2008b; Shiraiwa et al., 2008). The SP2 is well-suited to airborne measurements and has been previously used in the free troposphere (e.g. Schwarz et al., 2017 and references therein), though vertically resolved measurements in East Asia are sparse.

Only two previous aircraft campaigns (A-FORCE 2009 and A-FORCE W2013) measuring rBC included flights near the South Korean peninsula (Oshima et al., 2012; Kondo et al., 2016). These campaigns took place in the late winter (2013) and early spring (2009), meaning that South Korea was impacted by different large-scale meteorological patterns during the KORUS-AQ period than during previous measurements. Both local and trans-boundary pollution sources impact South Korea. South Korea has a high population density, particularly in the Seoul Metropolitan Area (SMA), which contains almost half (approximately 25.6 million people) of the country's population. Local pollution sources include industrial and urban emissions, ocean and shipping emissions, local biomass burning, and agricultural and biogenic emissions. Regional sources to South Korea include transport of industrial and agricultural burning emissions from China, erodible dust from central Asia, and wildfire emissions from Siberia. During the late spring, South Korea is typically impacted by long range transport from biomass burning in Siberia and dust transport from central Asia. The early summer period reflects the transition from westerly springtime Asian continental outflow to the Pacific (Clarke et al., 2004) to the late summer Asian monsoon season.

Here we focus on the vertically and spatially resolved BC observations from KORUS-AQ. These measurements can provide new constraints on the radiative effects of BC sourced in East Asia, and allow exploration of the observed variability of BC due to influences from different source regions. KORUS-AQ measurements and methodologies are described in Section 2. Section 3 examines chemical tracer relationships for air sourced to South Korea from different regions. Section 4 explores how source region and synoptic-scale meteorology impact the observed BC mass loadings, internal mixing, size distributions, and BC/CO relationship at different altitudes. In section 5, the source-dependence of vertically resolved BC mass loadings are used in conjunction with output from a global radiative transfer model (Samset & Myhre, 2011) to estimate relative contributions of different source regions to the regional BC direct radiative effect. These measurements are examined in the context of previous aircraft studies in the same region to assess how seasonal variability impacts BC concentrations at different altitudes.

2 Methods

2.1 Measurements in South Korea on the NASA DC-8

In situ measurements of rBC containing aerosols were made during the KORUS-AQ campaign on the NASA DC-8 aircraft. KORUS-AQ was an international air quality study which took place in South Korea from May 1st - June 10th, 2016, and employed a multi-platform approach to provide *in situ* sampling of aerosols and gases, with the over-arching goal of validating satellite and ground-based measurements of air quality (more information about KORUS-AQ is given in Al-Saadi et al. (2015)). The NASA DC-8 carried a suite of instruments to sample *in situ* aerosol composition, microphysics and optics, size distributions, and cloud droplets, as well as remotely sensed aerosol data products. Trace gas species and photolysis rates were also measured.

The DC-8 flew 20 research flights in South Korea, for a total of 154 flight hours, typically sampling between 300 to 7500 m over land and 150 to 7500 m over the ocean. Sampling targets included both the inflow and outflow regions of South Korea, with measurements over the Korean peninsula, the Yellow Sea, the East China Sea, and the Japan Sea (Figure 1). Systematic, repeated sampling over the Seoul Metropolitan Area (SMA) provided statistically robust measurements under different meteorological conditions, at different times of the day (Figure 1, inset). Most flights included an overflight of a ground site located in Olympic Park (central Seoul) followed by a missed approach (e.g. where the plane approaches a runway but does not complete a full-stop landing) at the Seoul Air Base (in Seongnam, directly southeast of Seoul), and then a spiral up to ~7500 m over the Taehwa Research Forest (a rural site near Gwangju, approximately 30 km southeast of Seoul), with this pattern repeated typically 3 times per flight, providing statistics for detailed analysis of vertical profiles without sampling bias.

rBC was detected with a single particle soot photometer (SP2, Droplet Measurement Technology, Longmont, CO), sampling from an iso-kinetic inlet mounted on the DC-8 (McNaughton et al., 2007), with typical sampling flow rates of ~2 vccm. The SP2 uses laser-induced incandescence to measure rBC mass on a single particle basis (Stephens et al., 2003). Single particle rBC mass is linearly proportional to its emitted incandescence signal (Slowik et al., 2007), which is detected by a photomultiplier tube (PMT). The rBC mass to incandescent signal relationship was calibrated using a BC reference material (Fullerene soot, Sigma-Aldrich lot #F12SO11) size-selected through a differential mobility analyzer (DMA) for mobility diameters between 125-350 nm. Previous inter-comparison studies demonstrated fullerene soot can be used as a consistent calibration standard for ambient rBC, as both similarly respond to laser induced incandescence (Kondo et al., 2011; Baumgardner et al., 2012). An empirical relationship between mobility diameter and single particle rBC mass was previously determined for SP2 measurements of fullerene soot (lot #F12SO11) (Moteki and Kondo, 2010). Mass calibrations with the DMA were performed 6 times during the campaign, and the average linear fit through all calibrations was used in processing data. The standard deviation between these calibrations gave an uncertainty in the single particle black carbon mass measurement of 6%/fg and a constant offset of <0.5 fg.

The volumetric rBC mass mixing ratio (MMR), reported in ng/(std. m^3), i.e. at standard pressure and temperature, was determined by adding up all single particle SP2 mass measurements in 1 second time bins and dividing by the measured sample flow rate, with an additional correction for the instrument's acquisition rate (Schwarz et al., 2006). The SP2's sampling flow rate was calibrated immediately preceding the campaign. Due to typical uncertainties in the flow rate during aircraft sampling and uncertainty in the relationship between the rBC reference material and ambient rBC mass, the rBC MMR measured by the SP2 has an estimated uncertainty of 25% (Schwarz et al. 2006; Laborde et al., 2012).

Since the SP2 measured rBC with a volume equivalent diameter of 100-500 nm (assuming a void-free density of 1.8 g/cm^3 for rBC), it quantified approximately 80-90% of rBC mass in the accumulation mode. To estimate total accumulation mode rBC mass (including rBC above and below the SP2 detection limit), a mass correction factor was determined from fitting a log normal distribution to the measured size distribution during each vertical sampling period (Spackman et al., 2008). These mass correction factors have been applied to the data in the vertical profile analysis discussed in Sections 3 and 4.

Preflight and inflight calibrations of the SP2 were made with polystyrene latex spheres (PSLs) to determine laser intensity for measurements of aerosol optical size from the scattered light signals measured by two avalanche photodiodes (Schwarz et al., 2010b). Mie core-shell theory was used to determine a coating thickness for materials internally mixed with rBC, using the leading-edge-only (LEO) fitting method (Gao et al., 2007), and assuming an index of refraction of $n_{coating}$=1.45 for the internally mixed material and n_{core}=2.26+1.26i (Moteki et al., 2010) for the rBC core. Uncertainty in core-shell lensing has previously been estimated to be ~10% for thickly coated particles, using laboratory generated aerosols; coatings on thinly coated rBC particles derived from LEO fitting may be underestimated by as much as 50% though (Ohata et al., 2016a). A temperature-dependent correction was applied to the measured scattering signal to account for decreased laser power at high temperatures, based on an observed correlation between PSL modal scattering signals and instrument temperature at the same laser current (See Supplementary Information Section S1 and Figure S1).

In this analysis, we have reported internal mixing of rBC in terms of an average coating thickness for particles containing 4-6 fg rBC cores; this criterion was adopted to maximize the number fraction of the rBC population included in the average (as the SP2 detected 4-6 fg rBC cores with high efficiency and the number distribution peaked below the SP2 mass detection limit of ~1 fg) and because optical sizing was typically achieved for greater than 90% of the number for rBC > 4 fg. This 4-6 fg rBC core range also allowed coatings to be compared between rBC populations with different size distributions. Observations from the SP2 were used to estimate absorption enhancement due to internal mixing for the population of detected rBC containing aerosols, as has been previously described in Schwarz et al. (2008b). This calculated absorption enhancement utilized both the coating thickness and rBC mass of individual particles, providing an estimate of the enhanced absorption (compared to bare BC) for the entire population of aerosols; as Mie core-shell theory was used, this is likely an overestimate (Liu et al., 2017).

In-cloud measurements, which can introduce artifacts related to inlet shattering by ice particles and cleansing of previously deposited materials by water droplets (Perring et al., 2013), have been removed from the data. Observation periods where clouds were likely present were determined from coarse mode measurements with a cloud particle spectrometer with polarization detection (CPSPD, Droplet Measurement Technology, Longmont, CO). Data associated with rapid changes in sampling pressure have also been removed, as derived rBC mass mixing ratios were directly impacted by uncertainties in the sampling flow rate.

In situ measurements of gas phase species that were co-emitted with BC were used in a chemical tracer analysis discussed in Section 3 to corroborate the back-trajectory analysis. Carbon monoxide gas was measured by the Differential Absorption Carbon Monoxide Measurement

(DACOM), with an uncertainty of 2% or 2 ppbv (parts per billion by volume), as described in Sachse et al., (1987; 1991). Acetonitrile (CH_3CN) and toluene (as well as other volatile organic carbon compounds) were measured by a proton transfer reaction-time-of-flight mass spectrometer (PTR-TOF-MS), with an uncertainty of ±20%, as described in Müller et al. (2014).

The Whole Air Sampler (WAS) collected ambient air during each flight into evacuated steel canisters over ~1-minute periods, approximately every 3-5 minutes. Trace gases, including halocarbons and hydrocarbons, were subsequently analyzed in a laboratory in California using gas chromatography with flame ionization detection, electron capture detection, and mass spectrometric detection, as described in Colman et al. (2001) and Simpson et al. (2011). Trichlorotrifluoroethane (CFC-113) was measured with a 3% accuracy and 1% precision. Dichloromethane (CH_2Cl_2) was measured with a 10% accuracy and 5% precision.

2.2 Back trajectory analysis of rBC sources

To investigate variability in vertically resolved BC mass and optical properties and relationships to trace gas species, a back-trajectory analysis was performed for all the NASA DC-8 flights to determine history of sampled air during the 5 days preceding sampling. 120-hour back trajectories were calculated using the Hysplit4 Model (NOAA's Hybrid Single-Particle Lagrangian Integrated Trajectory Model) (Draxler and Hess, 1997, 1998; Draxler et al., 1999; Stein et al., 2015), driven by meteorological data from the Global Data Assimilation System with a horizontal resolution of 0.5° and 55 vertical layers. Hysplit4 models back trajectories by interpolating meteorological data between grid points. Trajectory uncertainty can arise from starting position errors and uncertainty in the meteorological wind fields. Back trajectories were run for every minute of flight data in South Korea, initiated from the central values of altitude, latitude, and longitude sampled within that minute (9619 minutes total).

A source region was assigned to each observed air parcel by identifying the latitude and longitude associated with the most recent time the air parcel interacted with the boundary layer. The planetary boundary layer height was taken to be the model mixing depth (determined from the meteorological model at every point along each back trajectory). For air parcels observed within the boundary layer, they were assigned to the region in which they were measured, to provide an upper bound on the influence of local sources; to explore the inaccuracies in attributions due to this simple approach, several cases where the boundary layer was clearly influenced by transport from other regions are discussed in Sections 3 and 4.

Approximately one third of the back trajectories did not reach the boundary layer in the five days simulated. Since similarities between relationships of BC to co-emitted chemical tracers (Section 3.1) indicated these air parcels were likely significantly influenced by regional sources, they were instead associated with the region over which they spent the most time in the preceding 5 days; in 86% of cases, these were also the regions where air made the closest approach to the boundary layer. For air parcels that interacted with the boundary layer in less than 5 days, the average time since boundary layer interaction was 26.2 hours. This distribution of times until last boundary layer interaction showed clear diurnal trends, indicating that diurnal changes in planetary boundary layer height led to most interactions.

The position of last boundary layer interaction associated with all air parcels measured during vertical sampling above Taehwa Research Forest (discussed in Sections 4 and 5) is shown in

Figure 2 (5 day back trajectories are shown in Figure S3), along with defined regions used in this analysis. Higher altitude points are generally associated with longer-range transport, and with transport from lower latitudes. The regions used are South Korea, North Korea, marine/Japan, China, Russia, Mongolia, central Asia, and long-range transport. Marine/Japan designates back trajectories associated with boundary layer interactions over the East China Sea, Yellow Sea, Japan Sea and over Japan. Central Asia is defined as the region including Kazakhstan, Uzbekistan, Turkmenistan, Kyrgyzstan, and Tajikistan. Long range transport designates transport from any other region. Air parcels that did not interact with the boundary layer in the previous 5 days are not shown. The average time between sampling and last interaction with the boundary layer for South Korea was 5±10 hours (e.g. from 0-15 hours), North Korea 34±25 hours, marine/Japan 19±26 hours, China 45±26 hours, Russia 82±21 hours, Mongolia 61±19 hours, central Asia 94±15 hours, and long-range transport 93±19 hours.

We determined accumulated precipitation along the back trajectories (APT) by integrating hourly rainfall (in mm/hour, from the GDAS05 meteorological data fields) in a Lagrangian sense along each trajectory until its last interaction with the boundary layer. APT is a useful metric for evaluating which air parcels may have been influenced by precipitation and has previously been used in several studies to investigate the wet removal of aerosols (Matsui et al., 2011; Oshima et al. 2012; Kanaya et al. 2016).

3 Chemical tracer relationships for air sourced from different regions

3.1 rBC chemical tracer relationships

rBC-chemical tracer relationships for air sampled over South Korea associated with particular regions corroborated the back-trajectory analysis. Air parcels with enhanced toluene (which was observed to be very prevalent in urban areas of South Korea and has a chemical lifetime of ~2 days (Prinn et al., 1987)) were associated with South Korea, while those with significant CFC-113 were associated by the back-trajectory analysis with China (Vollmer et al., 2018).

The influences of different combustion sources and removal processes on BC were evaluated by studying co-emitted chemical species. Since both BC and CO are emitted during incomplete combustion, sources often have characteristic linear BC to CO relationships. Fresh biomass burning typically has a high BC/CO ratio, while more efficient urban combustion tends to have lower ratios of BC/CO (Spackman et al., 2008). Removal influences observed BC mass mixing ratios relative to CO, with higher BC/CO slopes indicative of fresher emissions, as BC is removed more rapidly than CO. Acetonitrile (CH_3CN) is also typically used as a tracer of biomass burning emissions (de Gouw et al., 2004; Warneke et al., 2004, 2006), although recent laboratory measurements also demonstrate CH_3CN can be emitted from residential coal burning (Cai et al., submitted). Dichloromethane (CH_2Cl_2) is a hydrocarbon that is not produced by combustion, but is used as an industrial solvent, and can be used as a tracer of urban emissions (Chen et al., 2007; Matsui et al., 2011).

The relationship between BC and CO, BC and CH_3CN, and BC and CH_2Cl_2 for each source region from average concentrations observed in the 1-minute time bins associated with each back-trajectory is shown in Figure 3 (CH_2Cl_2 is shown only during minutes when WAS observations were available, ~43% of observations). These tracer-tracer relationships indicated a significant mix of sources for air attributed to South Korea, China, and Marine/Japan, while transport from other regions generally demonstrated more linear tracer-tracer relationships. These linear trends were comprised of measurements over multiple observation days, not only associated with individual plumes. Observations attributed to regions based on residence time (shown as open circles) generally fell along the same trends as those attributed based on last interaction with the boundary layer (shown as filled circles).

The BC to CO relationship was highest for air associated with North Korea and with thinly coated rBC (<50 nm) in South Korea (3.9±0.2 ng/(std. m^3)/ppbv, R^2=0.68). These BC/CO relationships reflected both differences in BC/CO emission ratios, as well as the impact of removal during transport. The BC to CO ratio has previously been used to estimate removal efficiency in East Asia (Oshima et al., 2012), and long-term ground-based monitoring at Fukue Island provided estimates for characteristic BC/CO relationships for different source regions in East Asia, with more significant depletion in air that had a significant history of precipitation (Kanaya et al., 2016). As expected due to increasing likelihood of removal of BC with transport time, we note that increasing distance resulted in progressively lower BC/CO ratios. Long range transport in particular was associated with a slope of 1.3±0.1 ng/(std. m^3)/ppbv and an R^2=0.3, suggesting air mass mixing and BC removal during transport. This source region encompassed a wide geographical area, so combustion sources and removal events were likely highly inhomogeneous. While air sourced from Russia and from North Korea both typically entered South Korea from the north, the BC/CO associated with these two regions were distinct, with air sourced from Russia having a lower slope (2.7±0.1 vs. 3.2±0.2 ng/(std. m^3)/ppbv for North Korea).

South Korea showed significantly more air parcels associated with high BC loadings and little coatings than other regions, characteristic of freshly emitted BC near sources, and often associated with enhanced CH_2Cl_2, indicating urban sources. North Korea also demonstrated enhanced CH_2Cl_2 relative to BC.

Chinese-sourced air demonstrated two distinctive trends in BC/CH_3CN, with the higher slope (4.6±0.2, R^2=0.76) associated with back trajectories terminating near highly populated regions in northeastern and eastern China (e.g. with high observed BC concentrations associated with urban areas including Beijing and Shanghai), and the lower slope (0.47±0.03, R^2=0.54) associated with longer range transport from less populated areas in western and central China. The higher slope is associated with air masses that have a CH_3CN/CO slope of ~0.4 pptv/ppbv, which has recently been shown to be characteristic of combustion of bituminous coal typically used for residential cooking and heating in China (Cai et al., submitted). The air masses associated with northeastern and eastern China contain ~80% of the total BC MMR attributed to China during the campaign. The lower slope was likely associated with aged biomass burning. The BC/CH_3CN associated with western and central China was similar to that observed for long range transport, suggesting multiple influences for these air masses. The air masses from northeastern China also demonstrated a significant BC/CH_2Cl_2 correlation (1.6±0.1, R^2=0.63), consistent with this air being associated with urban regions.

3.2 Non-local influences in the boundary layer

The source attribution method (Section 2.2) used here cannot differentiate between local and non-local sources within the boundary layer. However, examination of differences in both BC-tracer relationships and BC microphysics has enabled identification of cases of clear non-local influence in the boundary layer. Observations of thickly coated rBC (>100 nm on average for 4-6 fg rBC cores) in air associated with Marine/Japan and with South Korea demonstrated a non-linear BC/CH_3CN trend (see Figure 3). These aerosols were observed on May 20th and 22nd, and back trajectories for these air masses suggested they were most likely influenced by aged smoke transported from fires in Siberia (see Figure S2 and Peterson et al. (2017) for more details). The Fire INventory from NCAR (FINN) (Wiedinmyer et al., 2011) indicated fires in this region of Siberia during the week preceding sampling. Since these measurements were generally at lower altitudes (<3 km), this case indicated significant mixing between air masses or influences of non-local sources for air sampled in the boundary layer was not fully captured by the source attribution method used here. We discuss further examples of non-local influence identified by differences in BC microphysics and mass loadings in Section 4.

4 Vertically resolved measurements over Taehwa Research Forest

The highest BC concentrations measured during the KORUS-AQ campaign occurred at low altitudes over the East China Sea and missed approaches at Seoul Air Base (up to 3700 ng/(std. m^3), while BC concentrations were lower over the Japan Sea (Figure 1). Within these broad patterns, however, changing meteorological conditions resulted in significant day-to-day variations. Here we have explored how distinct meteorological periods during the campaign influenced the observed rBC vertical profiles. We focused on spiral measurements over Taehwa Research Forest because the repeated sampling provided good statistics (48 rBC profiles comprising 874 minutes of flight time) and allowed us to avoid biases related to targeted sampling of plumes during some research flights.

4.1 rBC associated with different source regions over Taehwa Research Forest

Using the source region attribution described in Section 2.2 for the air parcels sampled over Taehwa Research Forest, the dM/dLogD mass distributions of rBC and the internal mixing (expressed as the average coating thickness for 4-6 fg rBC cores and as an absorption enhancement) associated with each source region were determined. The mass median diameter (MMD) of rBC associated with each region was found by fitting a log-normal distribution to the dM/dLogD mass distribution. These values are summarized in Table S1 along with the average coating thicknesses for 4-6 fg rBC cores and associated absorption enhancements. Normalized dM/dLogD mass distributions determined from the rBC core mass, expressed as a volume equivalent diameter are shown in Figure S4, as are normalized histograms of coating thickness for each source region. Uncertainty ranges for MMD and average coating thickness were determined from the standard deviation between values for every 10000 particles associated with each region; this bin size was chosen to provide sufficient statistics for the log-normal fits.

The MMD of rBC was related to both emission source and air parcel history since emission (Schwarz et al., 2008a; Moteki et al., 2012; Ohata et al., 2016b). On average the rBC associated with South Korea (and observed in the boundary layer, see Section 2.2) had the smallest mass median diameters (152±25 nm), characteristic of freshly emitted, urban rBC (Schwarz et al., 2008a). While air parcels associated with back trajectories only influenced by South Korea were relatively rare (Figure S3), this smaller MMD was consistent with observations on May 17th and

May 18th, where meteorological conditions limited transport, and rBC associated with South Korea in this case had an even smaller MMD of 130 nm. In general, the MMD associated with transported air from the other regions was larger (167-180 nm). The largest MMD was associated with rBC attributed to China (180±13 nm) and the Marine/Japan region (180±7 nm). The Marine/Japan region was generally influenced by transported pollution from China across the Yellow Sea. This larger MMD for rBC in air attributed to China was likely related to differences in combustion characteristics. This large size was consistent with measurements made during targeted sampling of Chinese pollution plumes in low legs over the Yellow Sea on May 25th, where a mass median diameter of 190 nm was measured in the marine boundary layer. For the selection of air masses associated with northeastern and eastern China, the MMD was 184±15 nm, while the MMD associated with western China was 170±5 nm, with a smaller mode at 435 nm (see Figure S5). These results were consistent with previous ground-based measurements on the northeastern Tibetan plain, where rBC has been observed to have a MMD of 175 nm, with a secondary MMD mode between 470-500 nm (Wang et al., 2014b). Other observations in China have also observed larger secondary modes (Huang et al., 2012; Wu et al., 2017). The mass median diameter associated with long range transport was smaller (167±11 nm) than any of the other regions excluding South Korea, which could be related to preferential removal of larger BC particles during transport (Ohata et al., 2016a). When considering all air parcels sampled during KORUS-AQ, the MMD decreased for air parcels associated with greater APT (accumulated precipitation, see Section 2.2), suggesting particles with greater rBC mass were more likely to be removed (Figure S6); however, this analysis was limited by the low number of observations associated with any particular source region.

The internal mixing of rBC particles, represented as both an average coating thickness and an absorption enhancement factor, also demonstrated variability related to source region. While the average coating thickness for South Korea was 75±25 nm, the histogram of coating thicknesses for South Korea (Figure S4) was bimodal, indicating mixed rBC populations with thinner and thicker coatings. Throughout the campaign, South Korean rBC generally included both thinner coatings (measured near sources, such as during the missed approaches at Seoul Air Base) and thicker coatings, which may be associated with significant secondary organic aerosol (SOA) formation observed within the Seoul Metropolitan Area (Kim et al., 2018). The average coatings observed during the missed approach at Seoul Air Base were typically <40 nm, and thinnest early in the day, characteristic of fresh urban emissions. For the observations on May 17th and 18th with minimal non-local influence, the average coating thickness was ~50 nm. As the Taehwa site was located downwind of Seoul, significant secondary formation of sulfate and organic aerosols leading to thicker rBC coatings on transported urban emissions was consistent with previous observations of increased rBC coatings downwind from urban and industrial sites (Moteki et al., 2007; Shiraiwa et al., 2007; Miyakawa et al., 2017). rBC sourced from China had thinner average coatings (71±11 nm) than air sourced from South Korea, but a narrower distribution, leading to a slightly higher absorption enhancement (1.66 vs. 1.64). The thickest average coatings (86±18 nm) and largest enhancement (1.79) were associated with the Marine/Japan region; this was likely related to aging as air was transported through the marine boundary layer far from source regions (including very thickly coated rBC sourced from wildfires in Siberia on May 20th and 22nd). Long range transport was associated with the thinnest coatings (60±4 nm) and lowest absorption enhancement (1.54), providing additional evidence for significant removal during transport. Consistent with laboratory measurements (McMeeking et al., 2010), air associated with a more significant history of precipitation (e.g. higher APT) was generally observed to have less thickly coated rBC than air with similar transport times to South Korea but with little history of precipitation (See Figure S6). The Mie theory core-shell calculation assumed the same index of refraction for the internally mixed "coatings" from all source regions and did not account for potential differences in chemical composition that could impact aerosol optical properties.

Several ground-based studies at Fukue Island, Japan have investigated source-region dependence of rBC optical properties and size distributions in East Asia. These included a study on Fukue Island in the spring (March and April) of 2007 (Shiraiwa et al., 2008), and more recent work on Noto Peninsula in the spring of 2013 (Ueda et al., 2016). Shiraiwa et al. (2008) observed larger rBC mass distributions in East Asian outflow (200-220 nm) than observed here. They also found that air attributed to China had smaller rBC mass distributions than South Korea or Japan. Disparities may be related to removal and atmospheric processing, which was likely more significant for the aerosols sampled above the boundary layer. Differences in hygroscopicity of aerosols sourced from different regions could also play a role, as internally mixed rBC sourced from China were shown to have undergone more efficient wet removal during transport than aerosols sourced from other regions (Miyakwa et al., 2017). Ground-based measurements were also more likely to be disproportionately influenced by near-source emissions or mixing in the boundary layer between local and transported emissions. Shiraiwa et al. found thinnest coatings for near-source and free tropospheric (unattributed) BC (2008), which were similar to the observation that both air attributed to South Korea and long-range transport had the thinnest observed coatings during KORUS-AQ. Ueda et al. (2016) also observed larger rBC mass distributions (183 to 217 nm) than our study, but similar to the observations presented here they found that transported rBC associated with China and the Yellow Sea had larger size distributions (210 and 217 nm) than nearer-source rBC from Japan or the Japan Sea (188 and 183 nm). Ueda et al. (2016) found absorption enhancements of ~1.3 for air sourced from China to Japan in the spring of 2013, although the enhancement reported here was not directly comparable since they determined enhancement from a thermodenuded photoacoustic soot spectrometer, while we calculated an enhancement via Mie theory.

4.2 Meteorological influences on vertically resolved BC source region

During the KORUS-AQ campaign, significant variation in large-scale (synoptic) meteorology influenced observed pollution levels in the study region, driven primarily by mid-latitude features. For this analysis, we defined four distinct meteorological periods: a "dynamic period", a "stagnant period", an "extreme pollution period", and a "blocking period" based on the observed synoptic meteorology. The "dynamic period" referred to the first two weeks of May, which were dominated by an active mid-latitude storm track responsible for pollution lofting, precipitation, and a significant dust transport event from China and Mongolia during May 4th-7th. This was followed by stagnant meteorological conditions ("stagnant period") dominated by persistent high pressure and weak synoptic flow, which magnified the impact of local pollution, from May 17th - May 22nd, and increased the importance of afternoon sea breezes in the Seoul area to facilitate boundary layer mixing. This period was also influenced by smoke transport from Siberia. The strongest impact of transported pollution from China ("extreme pollution period") occurred during May 25th - May 31st. This period included two distinct transport events, with the first from

May 25th until midday on May 28th, and a second less significant episode from May 29th-May 31st. A Rex Block ("blocking period") developed towards the end of the campaign, characterized by some pollution transport and cloud cover, from June 1st - June 7th. Rex Blocking occurs when a high-pressure weather system is located immediately north of a low-pressure system (in the northern hemisphere), blocking new weather systems from moving in, and creating fairly stable weather conditions in the impacted region (Rex, 1950). An overview of the meteorological conditions during the campaign were given in Peterson et al. (2017).

Each of these meteorological periods was represented in the vertical profiles over Taehwa Research Forest, with 16, 10, 9, and 8 vertical profiles during the dynamic, stagnant, extreme pollution, and blocking periods, respectively. The measured rBC concentration in ng/(std. m^3), coating thickness in nm (for 4-6 fg rBC cores), mass median diameter, and BC/CO slope for all 48 vertical profiles is shown in Figure 4, along with the average for each meteorological period.

Source attribution from the Hysplit back-trajectory analysis was used to investigate differences between meteorological period. Relative contributions of BC from each source region were determined in 50 hPa pressure bins for each period (Figure 5) by summing the rBC mass associated with that region and dividing by the total observed rBC mass in that altitude bin, for all vertical profiles measured during a specific meteorological period. Observed differences in vertical profiles during each meteorological period were associated with influences from different source regions. We determined the average and minimum/maximum boundary layer height during the observations over Taehwa for each of the 4 periods from the meteorological model. For each period we have also used the back-trajectory analysis to calculate the average APT associated with air sampled at different altitudes in 50 hPa bins (Figure S7).

For all meteorological periods, transport from China was generally significant between 900 hPa and 700 hPa, and at altitudes above 600 hPa; these distinct contributions were associated with transport from high population density areas in eastern and northeastern China at the lower altitudes, and transport from western and central China at the higher altitudes (see Figure 2 and Figure S3). Back trajectories for the extreme pollution period indicated that transported Chinese pollution observed at the lower altitude levels were typically sourced from further south (e.g. east central China) than during the other three meteorological periods. Russian sources were important between 700 and 450 hPa, but there was significant variability between meteorological periods. rBC loadings for profiles associated with Russia between 700 and 450 hPa generally had lower rBC concentrations than those from China: at 700 hPa, rBC loadings were typically < 50 ng/(std. m^3) in air attributed to Russia and >50 ng/(std. m^3) for air attributed to China. The fairly similar trends in APT associated with air sampled at these altitudes for each period indicated that differences in mass loadings reflected regional differences in emissions.
The dynamic period had the highest rBC MMR (Figure 4a) at altitudes above 600 hPa on average, although individual profiles showed significant variability, as this period was associated with the strongest vertical motion. In some cases, there were fairly high mass loadings at altitudes above 750 hPa, with concentrations near 100 ng/(std. m^3) even at the highest observed altitudes; these profiles were associated with back trajectories that had spent a significant amount of time over China, and in some cases, northern India. (The FINN inventory indicated significant fire activity in northern India at the beginning of the campaign.) The stagnant period was characterized by the lowest rBC MMR at all altitudes, save for the lowest bin, which had higher rBC MMR (670 ng/(std. m^3) at 1000 hPa) than during the dynamic (570 ng/(std. m^3)) and blocking (610 ng/(std. m^3)) periods, which was the result of large-scale subsidence. Like the dynamic period, this average profile was less variable above 750 hPa, although the average rBC MMR was much lower, approximately one-third of that observed during the dynamic period.
The highest rBC MMR was observed in the boundary layer during the extreme pollution period. The average value at 1000 hPa was 1400 ng/(std. m^3), more than twice the average during the other three periods; this suggests a significant influence of Chinese pollution at the surface, which was not captured by the source attribution method (Figure 5c). The highest rBC MMR found between 650-750 hPa was also observed during the extreme pollution period, averaging nearly twice what was observed at those altitudes during the other periods. This enhancement was associated with a larger relative contribution of Chinese pollution, which fell off above 600 hPa when long-range transport became dominant, leading to lower rBC MMR. Finally, the blocking period demonstrated a strong mix of both local and regional sources with less variability in the individual vertical profiles, possibly due to the blocking pattern creating a more stable atmospheric profile. The significant influence of Russian sources between 850 and 550 hPa corresponds with a less abrupt transition in the rBC mass vertical profile at these altitudes than during the other meteorological periods.

The average coating thickness (Figure 4b) during the dynamic period demonstrated more consistency than the rBC mass as a function of altitude and was characterized by thinner coatings on rBC (at all altitudes) than the other meteorological periods. Since there were several rain events during this two-week period, wet removal may have preferentially removed thickly coated particles. The average APT was not significantly different than the other meteorological periods, however, suggesting the short timing between rain events may have been an important factor.
The average rBC coatings near the surface were thickest during the stagnant period, likely due to

secondary aerosol formation increasing the coatings on aged local pollution. The thickest coated rBC near the surface (>100 nm) was measured during the flight on May 22nd (as noted previously, this was likely due to aged, transported smoke from biomass burning in Siberia). For the extreme pollution period, the coatings showed enhancements between 1000-750 hPa, although they were thinner above 600 hPa (similar to the dynamic period), likely due to the influence of long-range transport and wet removal (see Figure S7). The blocking period was characterized by rBC coatings that showed an enhancement between 700 and 500 hPa, which was associated with transport from both China and Russia, as well as less significant contributions from Mongolia and Central Asia. This enhancement also corresponds with less APT (on average) associated with air sampled at those altitudes than during the other meteorological periods.

In general, the MMD (Figure 4c) was lowest near the surface, increased up to approximately 750 hPa, and then declined slightly from 750 hPa to 400 hPa. From the surface up to 750 hPa this trend was related to the dominance of rBC sourced from South Korea, with other sources becoming increasingly important at higher altitudes. The slight decline in MMD from 750 hPa to 400 hPa was likely due to preferential removal of larger BC particles in transported air. Average APT for sampled air increased relative to altitude during all meteorological periods (Figure S7). The blocking period, which was less influenced by long range transport than the dynamic period, showed a larger MMD at these altitudes.

The BC to CO relationship (Figure 4d) also demonstrated progressive removal at higher altitudes, as the highest BC/CO was generally observed near the surface. In some cases, plumes with higher relative BC/CO were observed in upper altitude bins, likely indicating instances of efficient transport from source regions with minimal removal. The highest BC/CO were attributed to air masses associated with low APT, indicating wet removal during transport significantly influenced the observed mass loadings (Figure S7). The highest BC/CO at all altitudes was observed during the stagnant period, which may be related to the influence of aged biomass burning smoke from Siberia (generally attributed to the marine/Japan region, see Figure 5b and Figure S2).

5 Observationally constrained influences on the BC direct radiative effect over South Korea

To estimate the influence of different source regions on the BC direct radiative effect (DRE) in South Korea, we used the Hysplit back trajectory analysis to assess their relative contributions to BC vertical concentration profiles over Taehwa Research Forest (Figure 6, right panel). Since this analysis included all 48 vertical profiles measured during the campaign, it was not directly comparable to the relative contributions presented in Figure 5, as not every observation could be stratified into a specific meteorological period. The inferred relative contributions were then combined with an altitude-dependent normalized direct radiative forcing derived from a global radiative transfer model (discussed in Section 5.1) to calculate the source-specific BC DRE over South Korea. The BC DRE has previously been shown to be influenced by surface albedo, cloud cover, cloud height, BC mass loadings and microphysics, and the thermal structure of the atmosphere (Hodnebrog et al., 2014; Samset & Myhre, 2015; Stjern et al., 2017); our analysis here neglects these issues. While this analysis does not provide a rigorous determination of the

BC DRE specific to the actual metrological conditions during measurement, it does enable evaluation of altitude-resolved contributions from different regions to both the DRE and DRE-variability driven only by BC mass.

5.1 BC normalized direct radiative effect

A global radiative transfer model previously described in Samset and Myhre (2011) was used to estimate the regional normalized direct radiative forcing (NDRF) efficiency for black carbon during KORUS-AQ. The NDRF is defined as the impact of aerosols (normalized by mass) at a particular altitude level on the outgoing, top-of-the-atmosphere shortwave flux, and has been used in several studies to explore the sensitivity of the DRE to variations in the vertical distribution of aerosols (Zarzycki & Bond, 2010; Samset & Myhre, 2011). This impact increases as a function of altitude (Figure 6 left panel, dashed black line) with the strongest effect associated with aerosols at the highest altitudes reflecting the fact that absorbing aerosols above clouds have a higher radiative impact than those in clear sky or below clouds (Stier et al., 2006; Zarzyki & Bond, 2010). To provide a climatological treatment of this issue, the radiative transfer model was run with regionally and seasonally resolved cloud conditions using the Integrated Forecast System at the ECMWF (Myhre et al., 2009). NDRF values were determined from an average over May and June for SMA (variability in DRE was evaluated for day-to-day changes in mass loadings, but not in cloud cover). The model assumed a MAC of 7.5 m^2/g at 550 nm for all BC and aged BC was assumed to be internally mixed with 50% higher absorption than fresh BC, although these values were not observationally constrained.

We determined the column DRE for BC at the top of the atmosphere by multiplying the observed rBC mass burden with the NDRF at that altitude and integrating over all altitude bins (from 1000 hPa to 50 hPa). Since there were generally no observations over Taehwa Research Forest above 400 hPa, two limiting cases for the higher altitude mass loadings were used to estimate the possible range of the un-measured fraction on NDRF. There were 3 observations during KORUS-AQ up to ~250 hPa; these vertical profiles are shown in Figure S8 and indicated rBC MMR of ~7 ng/(std. m^3) at 250 hPa in the region. For a central estimate, we therefore assumed the rBC MMR decreases linearly from the observation at 400 hPa to 7 ng/(std. m^3) at 250 hPa (as the default case). For an upper bound, based on observations at 400 hPa that had significantly higher mass loadings than these 3 observations, we assumed bins from 400 hPa up to 200 hPa had the same mass mixing ratio as at 400 hPa, consistent with previous observations that indicated common occurrence of stable profiles for these altitudes (Schwarz et al., 2017). For the upper bound case above 200 hPa, we assumed an rBC mass mixing ratio of 1 ng/m^3 (~4 ng/(std. m^3), consistent with previous observations of high altitude rBC (Schwarz et al., 2006; Murphy et al., 2014). The altitude to pressure relationship above 400 hPa was estimated from the US standard atmosphere model.

5.2 Diurnal and meteorological variability

The total and relative regional contributions to the DRE from BC determined from this analysis are summarized in Table 1 for both the campaign average and each of the four meteorological periods. The column DRE over Taehwa Research Forest was between 0.48 and 1.86 W/m^2 during the measurement period, with an average value of 0.96 W/m^2. If we included the data for the entire Seoul Metropolitan Area (SMA) in this analysis (e.g. including surface loadings measured during the missed approaches at Seoul Air Base, which extended below vertical profiling over Taehwa), the average regional DRE for SMA was estimated to be slightly higher, at 1.04 W/m^2 (0.51 to 2.01 W/m^2). The relative contributions from each region were determined by integrating the percentage of the rBC burden associated with that region with the NDRF efficiency of its associated altitude. The assumed rBC mass burden in the high-altitude bins above 400 hPa up to 50 hPa using the central estimate accounted for on average 12% of the total campaign averaged DRE. Using the upper bound estimate for the high-altitude mass loadings, the column DRE was 10% higher, at 1.05 W/m^2 (0.52 to 1.90 W/m^2), with the high-altitude aerosols accounting for 19% of the total.

The four meteorological periods exhibited different column DRE, with the extreme pollution period having the highest average DRE (1.50 W/m^2). If we assumed that the rBC MMR measured in the boundary layer (at altitudes less than 800 hPa) that exceeded the average contributions from the other three meteorological periods was associated with Chinese transport (see Figure 4a), the relative contributions to the DRE for South Korea and China were 17% and 39% respectively. The Stagnant period also had a significant impact from China aloft, but the lowest DRE (0.67 W/m^2) of the four periods; a significant portion of the contribution associated with Marine/Japan (21%) was likely related to Siberian smoke transport in the marine boundary layer. The dynamic period (0.92 W/m^2) was the most variable, both because it spanned the longest time period and also because of variability in high altitude rBC MMR (Figure 4a), which were sometimes a significant portion of the total column DRE. While the blocking period (0.91 W/m^2) had a similar average to the dynamic period, it had a different mix of sources above the boundary layer, including some contributions from North Korea, but little from long range transport (Figure 5d). To estimate how observed absorption enhancement would impact the BC DRE, we scaled the mass burden by the SP2-determined absorption enhancement relative to the 1.5x enhancement already assumed in the NDRF calculation (effectively scaling the mass absorption coefficient). Scaling to the observed absorption enhancement led to a higher campaign average DRE (1.14 W/m^2), and greater variability in DRE between the meteorological periods: the average for the dynamic period was 1.03 W/m^2, the stagnant period 0.87 W/m^2, the extreme pollution period 1.80 W/m^2, and the blocking period 1.08 W/m^2. This estimate did not account for changes in BC lifetime, which we assumed to be negligible over the limited geographical region we considered here.

The variability in the total column DRE was determined from the minimum and maximum of the 48 observations on 20 different flight days (see Figure S9 for DRE of individual profiles and relative contributions by source region). For profiles that did not have measurements in the lowest altitude bins, we used the campaign averaged BC mass and relative contributions for those bins, which may affect the accuracy of values for individual profiles but not the campaign average. Relative contributions also cannot be assessed with high resolution for individual profiles, as each profile only included ~17 minutes of data. Nevertheless, the large variability in regional DRE was clearly associated with either changes in the relative contributions of rBC sourced from China or from high mass loadings at the highest observed altitudes (Table 1 and SI Figure S9). The vertical profiles with the highest DRE values were generally those that were strongly impacted by contributions from China (e.g. during the period of extreme pollution and on May 2nd and May 5th); in some cases there were also significant contributions from high altitude loadings (on May 2nd, May 5th, and May 26th). Diurnal trends for same-day observations generally showed increasing South Korean contributions throughout the day (on May 7th, May

12^{th}, May 18^{th}, May 20^{th}, May 30^{th}, June 2^{nd} and June 9^{th}), often with an associated increase in DRE, likely due to mixing of local emissions to higher altitudes, where their radiative impact was amplified.

The NDRF values determined in Samset and Myhre (2011) were strongly dependent on cloud conditions, with cloud effects largely responsible for the strong vertical trend in NDRF. Estimating these effects on a profile by profile basis is beyond the scope of this work, but observed differences in cloud cover between meteorological periods suggest that variability in DRE from this source would be larger than would be estimated from the concentration variability. In general, cloud cover was highest during the dynamic period and blocking period, with significant cloud cover at the end of the stagnant period and beginning of the extreme pollution period (Peterson et al., 2017). The clearest sky conditions were observed during the stagnant period, which corresponded with the lowest estimated DRE from the mass variability alone (Table 1).

5.3 Spatial and seasonal variability of rBC vertical profiles

Previous vertically resolved rBC measurements near the South Korean peninsula made during the A-FORCE campaigns taken in conjunction with these observations provide extended information about the seasonal variability of the BC direct radiative effect in the region. A-FORCE 2009 made observations in early spring, from March 18^{th} to April 25^{th}, 2009, and A-FORCE W2013 made observations in late winter, between February 14^{th} and March 10^{th}, 2013. Details of the measurements and flights during these campaigns were given in Oshima et al. (2012) and Kondo et al. (2016). Seasonal differences in BC mass concentrations in East Asia during these two campaigns were previously discussed in Kondo et al. (2016). Collocated measurements over the Yellow Sea during KORUS-AQ and the A-FORCE campaigns were used to evaluate seasonal changes in vertical BC mass burden. The A-FORCE 2009 campaign had 78 profiles between 31-38°N and 123-131°E, close to the Korean peninsula; the A-FORCE W2013 campaign had 63 profiles in the same location (See Figure 7 for vertical profile locations). Since measurements over the Yellow Sea during KORUS-AQ were generally targeting periods of significant continental outflow, the observed mass burden may overestimate the true seasonal average.

We compared the average mass burden of a subset of these measurements, between 33-38°N and 123.6-125.6°E, where measurements during all 3 campaigns were in nearly the same location (Figure 7). Surface loadings over the Yellow Sea were lower during the KORUS-AQ observations, but the measurements during the spring A-FORCE 2009 campaign demonstrated statistically significant higher mass loadings at the upper altitudes, above 700 hPa. The A-FORCE 2013W campaign measured higher mass loadings between 900 and 700 hPa, but a similar rBC mass burden above 700 hPa. The spatial variability between average profiles of rBC MMR during the A-FORCE and KORUS-AQ campaigns in other regions (where vertical sampling periods were not completely co-located) is shown in Figures S10 and S11.

The difference between the A-FORCE campaigns and KORUS-AQ could be due to year-to-year variability, but emission inventories from 2009 to 2013 (the last year included) showed increasing trends in regional BC emissions (Granier et al., 2017), suggesting the difference may be due to changes in seasonal transport. The earlier part of the KORUS-AQ campaign also demonstrated higher altitude rBC loadings than observed in the latter part of the campaign, suggesting changing seasonal transport patterns. In terms of the BC DRE, the greater observed rBC mass burden above 700 hPa during the A-FORCE 2009 campaign may be offset somewhat by the lower regional NDRF at these altitudes during the early spring (see Figure 7, right panel), but a detailed analysis of the seasonal variability of regional DRE is beyond the scope of this work.

6 Discussion and Conclusions

This study investigated BC observed over South Korea during the KORUS-AQ campaign. These measurements provide a benchmark for future changes in regional BC emissions in East Asia. We explored the observed variability in rBC vertical profiles over a single site in South Korea over ~6 weeks. BC measurements coupled with a back-trajectory analysis demonstrated that both local and regional sources influenced the observed aerosol loadings, with significant vertical stratification of source contributions and variability attributable to meteorologically-driven changes in transport and removal. Model results are strongly dependent on their representation of BC's vertical concentration profiles (Samset et al. 2013), and here we investigated how much real variability in BC profiles over a single location impacted BC DRE.

These vertically resolved measurements suggest that BC transported from regional sources to South Korea were responsible for the majority of the regional DRE over South Korea, due in part to the larger forcing efficiency associated with higher altitude BC. Due to its location and geographic size, the importance of transboundary BC for regional DRE in South Korea was unsurprising, in contrast to neighboring China (where 65% of the annual BC regional DRE was attributed to local emissions in a modeling study (Yang et al., 2017)). Although previous work has shown that emissions from highly populated areas in northeastern China can contribute significantly to South Korea's regional DRE (Kim et al., 2012), these measurements suggested that in late spring Russia's relative contribution to the regional DRE over South Korea may also be important; the misattribution of air masses likely influenced by aged smoke transported from Siberia in this analysis suggested that Russia's influence could be more significant than was estimated here. Since relative contributions were determined for altitudes below 400 hPa, contributions from long range transport were also likely underestimated.

The estimated values for regional DRE in South Korea (0.48-1.86 W/m^2) were similar to those derived in modeling studies. For example, Kim et al. (2012) estimated a regional DRE between 0.4 and 1.8 W/m^2 in the Seoul Metropolitan Area. The 3D radiative transfer modeling analysis in Matsui et al. (2016a) found higher regional DRE values (1.6-2.8 W/m^2 for spring 2009), but their study included eastern China in the model domain, suggesting the analysis presented here provided a reasonable estimate of DRE. Previous studies using NDRF have generally found good agreement with global 3-D model estimates (Zarzycki & Bond, 2010). The NDRF values given by the model used in this analysis (Samset & Myhre, 2011) were generally strong compared to other radiative forcing model estimates (Samset & Myhre, 2015; Myrhe & Samset, 2015).

The analysis in Section 5 also highlighted the importance of constraining BC in the upper troposphere. Even in a strong source region like East Asia, the upper altitude aerosols (above 400 hPa) could account for up to one fifth of the BC direct radiative effect on average. We take this number as an upper limit but note significant uncertainty in constraining the regional DRE in East Asia with aircraft observations. This observation is consistent with previous modeling studies that have noted a significant fraction of the uncertainty in modeled BC DRE is due to higher altitude aerosols (Samset et al. 2013; Wang et al. 2014a). The high rBC mass loadings associated with strong vertical motion observed at the beginning of the campaign indicated that upper altitude aerosols may be significant in the region in certain cases.

Although we have estimated the DRE associated with BC over South Korea, the climate impacts of BC do not directly scale with DRE. The total climatic impact of BC also depends on rapid adjustments to the absorption and heating throughout the atmospheric column. These adjustments work against the DRE, lowering the effective radiative effect, but also altering the lapse rate and cloud properties (Hodnebrog et al., 2014; Samset & Myhre, 2015; Stjern et al., 2017). These measurements indicated that BC size distributions and optical properties were influenced by source region in East Asia. This also has implications for the regional BC climate impacts, including source-specific BC lifetime, removal, and cloud effects, since larger BC is more likely to act as good cloud condensation nuclei (McMeeking et al., 2011).

Although this study demonstrated that both local and regional sources influenced BC regional climate effect over South Korea, contributions to the observed rBC surface loadings are important for local air quality. Note that BC was a significant portion of the PM1 mass (~7% from ground-based measurements in SMA during KORUS-AQ (Kim et al., 2018)). During this observation period, the significantly higher mass loadings associated with the extreme pollution period suggested that BC transported from China impacted surface loadings at Taehwa in some cases. However, the consistent average values for the rBC MMR observed at the surface during the other three periods (including cases where no back trajectories were associated with highly populated regions of China) indicated significant local contributions as well.

In addition to investigating the variability in rBC vertical profiles over a single site near a megacity in East Asia, these measurements provided a more complete picture of the spatial gradients in rBC for the inflow and outflow regions of South Korea (Figure S11). Vertically resolved measurements of rBC demonstrated significant spatial variability across a relatively small region at all altitudes. The disconnect between *in situ* observations and the coarse spatial resolution typically used by global aerosol models leads to substantial sampling errors even when using observations that “perfectly” agree with models (on the order ~100% for instantaneous BC surface loadings) (Schutgens et al., 2016). Since global climate models including aerosols can use grid spacing of ~200 km, and even satellite observations typically have resolutions ~10 km, the observed spatial variability would be challenging to constrain with current aerosol models and remote observations.

The temporal variability associated with vertical sampling over a single site monitored over multiple days and meteorological conditions indicated a further challenge for global aerosol models, as short-term meteorological conditions and variability in source regions significantly influenced observations. These measurements demonstrated that diurnal and day-to-day variability in absorbing aerosol mass loadings and optical properties were significant, although many aerosol models provide output only on broad temporal scales, such as monthly averages. A study on the variability of aerosol loadings, composition, and relative humidity in systematic, repeated vertical sampling during the DISCOVER-AQ campaign in the Baltimore-Washington D.C. area demonstrated that significant model biases arise from averaging aerosol optical properties on daily or monthly timescales (Beyersdorf et al., 2016). Both the temporal variability associated with synoptic-scale meteorology and the diurnal variability in the column BC DRE during KORUS-AQ was observed to be as much as a factor of 2.

Acknowledgments and Data

We would like to thank the NASA DC-8 pilots and crew for their important role in obtaining the data used in this analysis. We would also like to acknowledge the contributions of the KORUS-AQ science team, particularly Dr. Joon-Young Ahn for his contributions to the SP2 measurements on the NASA DC-8. The NOAA SP2 data were obtained and analyzed with the support of the NASA Radiation Sciences Program, the NASA Upper Atmosphere Research Program, and the NOAA Atmospheric Composition and Climate Program.

PTR-MS measurements aboard the NASA DC-8 during KORUS-AQ were supported by the Austrian Federal Ministry for Transport, Innovation and Technology (bmvit) through the Austrian Space Applications Programme (ASAP) of the Austrian Research Promotion Agency (FFG). The PTR-MS instrument team (P. Eichler, L. Kaser, T. Mikoviny, M. Müller) is acknowledged for their support. B.A.N. and P.C.J. would like to thank NASA NX15AT96G for support.

K.D.L. would like to thank Ken Aikin, Eric Ray, and Owen Cooper for useful discussion on the regional analysis.

Data for the KORUS-AQ campaign are publicly available at https://www-air.larc.nasa.gov/cgi-bin/ArcView/korusaq

Data from the A-FORCE campaigns are publicly available at https://doi.org/10.5281/zenodo.1444094

References

Adler, G., Riziq, A.A., Erlick, C. & Rudich, Y. (2010). Effect of intrinsic organic carbon on the optical properties of fresh diesel soot. *Proceedings of the National Academy of Sciences*, *107*(15), pp.6699-6704.

Al-Saadi, J., Carmichael, G. & Crawford, J. (2016). NASA Contributions to KORUS-AQ: An International Cooperative Air Quality Field Study in Korea. NASA; 2015.

Baumgardner, D., Popovicheva, O., Allan, J., Bernardoni, V., Cao, J., Cavalli, F., et al. (2012). Soot reference materials for instrument calibration and intercomparisons: a workshop summary with recommendations. *Atmospheric Measurement Techniques*, *5*, pp.1869-1887.

Beyersdorf, A.J., Ziemba, L.D., Chen, G., Corr, C.A., Crawford, J.H., Diskin, G.S., et al. (2016). The impacts of aerosol loading, composition, and water uptake on aerosol extinction variability in the Baltimore–Washington, DC region. *Atmospheric Chemistry and Physics*, *16*(2), pp.1003-1015.

Bond, T.C., Doherty, S.J., Fahey, D.W., Forster, P.M., Berntsen, T., DeAngelo, et al. (2013). Bounding the role of black carbon in the climate system: A scientific assessment. *Journal of Geophysical Research: Atmospheres*, *118*(11), pp.5380-5552.

Cai, S., L. Zhu, S. Wang, A. Wisthaler, Q. Li, J. Jiang, & J. Hao, Time-resolved intermediate and semi-volatile organic compounds emissions from household coal combustion in northern China, submitted to *Environmental Science and Technology*.

Cappa, C.D., Onasch, T.B., Massoli, P., Worsnop, D.R., Bates, T.S., Cross, E.S., et al. (2012). Radiative absorption enhancements due to the mixing state of atmospheric black carbon. *Science*, *337*(6098), pp.1078-1081.

Chen, M., Talbot, R., Mao, H., Sive, B., Chen, J. & Griffin, R.J. (2007). Air mass classification in coastal New England and its relationship to meteorological conditions. *Journal of Geophysical Research: Atmospheres*, *112*(D10).

Clarke, A.D., Shinozuka, Y., Kapustin, V.N., Howell, S., Huebert, B., Doherty, S., et al. (2004). Size distributions and mixtures of dust and black carbon aerosol in Asian outflow: Physiochemistry and optical properties. *Journal of Geophysical Research: Atmospheres*, *109*(D15).

Colman, J.J., Swanson, A.L., Meinardi, S., Sive, B.C., Blake, D.R. & Rowland, F.S. (2001). Description of the analysis of a wide range of volatile organic compounds in whole air samples collected during PEM-Tropics A and B. *Analytical Chemistry*, *73*(15), pp.3723-3731.

De Gouw, J.A., Cooper, O.R., Warneke, C., Hudson, P.K., Fehsenfeld, F.C., Holloway, J.S., et al. (2004). Chemical composition of air masses transported from Asia to the US West Coast during ITCT 2K2: Fossil fuel combustion versus biomass-burning signatures. *Journal of Geophysical Research: Atmospheres*, *109*(D23).

Draxler, R.R. (1999). *HYSPLIT4 user's guide. NOAA Air Resources Laboratory, Silver Spring, MD*. NOAA Tech. Memo.

Draxler, R.R. & Hess, G.D. (1997). Description of the HYSPLIT-4 Modeling System. NOAA Technical Memorandum ERL ARL-224, NOAA Air Resources Laboratory, Silver Spring, 1-24.

Draxler, R.R. & Hess, G.D. (1998). An overview of the HYSPLIT_4 modelling system for trajectories. *Australian meteorological magazine*, *47*(4), pp.295-308.

Gao, R.S., Schwarz, J.P., Kelly, K.K., Fahey, D.W., Watts, L.A., Thompson, T.L., et al. (2007). A novel method for estimating light-scattering properties of soot aerosols using a modified single-particle soot photometer. *Aerosol Science and Technology*, *41*(2), pp.125-135.

Granier, C., Doumbia, T., Granier, L., Sindelarova, K., Frost, G.J., Bouarar, I., et al. (2017). Anthropogenic Emissions in Asia. In *Air Pollution in Eastern Asia: An Integrated Perspective* (pp. 107-133). Springer, Cham.

Hadley, O.L., Ramanathan, V., Carmichael, G.R., Tang, Y., Corrigan, C.E., Roberts, G.C. & Mauger, G.S. (2007). Trans-Pacific transport of black carbon and fine aerosols (D< 2.5 μm) into North America. *Journal of Geophysical Research: Atmospheres*, *112*(D5).

Hodnebrog, Ø., Myhre, G. & Samset, B.H. (2014). How shorter black carbon lifetime alters its climate effect. *Nature communications*, *5*, p.5065.

Huang, X.F., Sun, T.L., Zeng, L.W., Yu, G.H. & Luan, S.J. (2012). Black carbon aerosol characterization in a coastal city in South China using a single particle soot photometer. *Atmospheric environment*, *51*, pp.21-28.

Jacobson, M.Z. (2001). Strong radiative heating due to the mixing state of black carbon in atmospheric aerosols. *Nature*, *409*(6821), p.695.

Kanaya, Y., Pan, X., Miyakawa, T., Komazaki, Y., Taketani, F., Uno, I. & Kondo, Y. (2016). Long-term observations of black carbon mass concentrations at Fukue Island, western Japan, during 2009–2015: constraining wet removal rates and emission strengths from East Asia. *Atmospheric Chemistry and Physics*, *16*(16), pp.10689-10705.

Kim, M.Y., Lee, S.B., Bae, G.N., Park, S.S., Han, K.M., Park, R.S., et al. (2012). Distribution and direct radiative forcing of black carbon aerosols over Korean Peninsula. *Atmospheric environment*, *58*, pp.45-55.

Kim, H., Zhang, Q. & Heo, J. (2018). Influence of intense secondary aerosol formation and long-range transport on aerosol chemistry and properties in the Seoul Metropolitan Area during spring time: results from KORUS-AQ. *Atmospheric Chemistry and Physics*, *18*(10), pp.7149-7168.

Kipling, Z., Stier, P., Johnson, C.E., Mann, G.W., Bellouin, N., Bauer, S.E., et al. (2016). What controls the vertical distribution of aerosol? Relationships between process sensitivity in HadGEM3–UKCA and inter-model variation from AeroCom Phase II. *Atmospheric Chemistry and Physics*, *16*(4), pp.2221-2241.

Kondo, Y., Sahu, L., Moteki, N., Khan, F., Takegawa, N., Liu, X., et al. (2011). Consistency and traceability of black carbon measurements made by laser-induced incandescence, thermal-optical transmittance, and filter-based photo-absorption techniques. *Aerosol Science and Technology*, *45*(2), pp.295-312.

Kondo, Y., Moteki, N., Oshima, N., Ohata, S., Koike, M., Shibano, Y., et al. (2016). Effects of wet deposition on the abundance and size distribution of black carbon in East Asia. *Journal of Geophysical Research: Atmospheres*, *121*(9), pp.4691-4712.

Laborde, M., Mertes, P., Zieger, P., Dommen, J., Baltensperger, U. & Gysel, M. (2012). Sensitivity of the Single Particle Soot Photometer to different black carbon types. *Atmospheric Measurement Techniques*, *5*(5), p.1031.

Liu, D., Whitehead, J., Alfarra, M.R., Reyes-Villegas, E., Spracklen, D.V., Reddington, C.L., et al. (2017). Black-carbon absorption enhancement in the atmosphere determined by particle mixing state. *Nature Geoscience*, *10*(3), pp.184-188.

Matsui, H., Kondo, Y., Moteki, N., Takegawa, N., Sahu, L.K., Zhao, Y., et al. (2011). Seasonal variation of the transport of black carbon aerosol from the Asian continent to the Arctic during the ARCTAS aircraft campaign. *Journal of Geophysical Research: Atmospheres*, *116*(D5).

Matsui, H. (2016a). Black carbon simulations using a size-and mixing-state-resolved three-dimensional model: 1. Radiative effects and their uncertainties. *Journal of Geophysical Research: Atmospheres*, *121*(4), pp.1793-1807.

Matsui, H. (2016b). Black carbon simulations using a size-and mixing-state-resolved three-dimensional model: 2. Aging timescale and its impact over East Asia. *Journal of Geophysical Research: Atmospheres*, *121*(4), pp.1808-1821.

McMeeking, G.R., Good, N., Petters, M.D., McFiggans, G. & Coe, H. (2011). Influences on the fraction of hydrophobic and hydrophilic black carbon in the atmosphere. *Atmospheric Chemistry and Physics*, *11*(10), pp.5099-5112.

McNaughton, C.S., Clarke, A.D., Howell, S.G., Pinkerton, M., Anderson, B., Thornhill, L., et al. (2007). Results from the DC-8 Inlet Characterization Experiment (DICE): Airborne versus surface sampling of mineral dust and sea salt aerosols. *Aerosol science and technology*, *41*(2), pp.136-159.

Miyakawa, T., Oshima, N., Taketani, F., Komazaki, Y., Yoshino, A., Takami, A., et al. (2017). Alteration of the size distributions and mixing states of black carbon through transport in the boundary layer in east Asia. *Atmospheric Chemistry and Physics*, *17*(9), pp.5851-5864.

Moteki, N., Kondo, Y., Miyazaki, Y., Takegawa, N., Komazaki, Y., Kurata, G., et al. (2007). Evolution of mixing state of black carbon particles: Aircraft measurements over the western Pacific in March 2004. *Geophysical Research Letters*, *34*(11).

Moteki, N. & Kondo, Y. (2010). Dependence of laser-induced incandescence on physical properties of black carbon aerosols: Measurements and theoretical interpretation. *Aerosol Science and Technology*, *44*(8), pp.663-675.

Moteki, N., Kondo, Y. & Nakamura, S.I. (2010). Method to measure refractive indices of small nonspherical particles: Application to black carbon particles. *Journal of Aerosol Science*, *41*(5), pp.513-521.

Moteki, N., Kondo, Y., Oshima, N., Takegawa, N., Koike, M., Kita, K., et al. (2012). Size dependence of wet removal of black carbon aerosols during transport from the boundary layer to the free troposphere. *Geophysical Research Letters*, *39*(13).

Moteki, N., Adachi, K., Ohata, S., Yoshida, A., Harigaya, T., Koike, M. & Kondo, Y. (2017). Anthropogenic iron oxide aerosols enhance atmospheric heating. *Nature Communications*, *8*.

Müller, M., Mikoviny, T., Feil, S., Haidacher, S., Hanel, G., Hartungen, E., et al. (2014). A compact PTR-ToF-MS instrument for airborne measurements of volatile organic compounds at high spatiotemporal resolution. *Atmospheric Measurement Techniques*, *7*(11), pp.3763-3772.

Murphy, D.M., Froyd, K.D., Schwarz, J.P. & Wilson, J.C. (2014). Observations of the chemical composition of stratospheric aerosol particles. *Quarterly Journal of the Royal Meteorological Society*, *140*(681), pp.1269-1278.

Myhre, G., Berglen, T. F., Johnsrud, M., Hoyle, C. R., Berntsen, T. K., Christopher, S. A., et al. (2009). Modelled radiative forcing of the direct aerosol effect with multi-observation evaluation, *Atmospheric Chemistry and Physics*, 9, 1365-1392, https://doi.org/10.5194/acp-9-1365-2009.

Myhre, G., Samset, B.H., Schulz, M., Balkanski, Y., Bauer, S., Berntsen, T.K., et al. (2013). Radiative forcing of the direct aerosol effect from AeroCom Phase II simulations. *Atmospheric Chemistry and Physics*, *13*(4), p.1853.

Myhre, G. & Samset, B.H. (2015). Standard climate models radiation codes underestimate black carbon radiative forcing. *Atmospheric Chemistry and Physics*, *15*(5), pp.2883-2888.

Ohata, S., Schwarz, J.P., Moteki, N., Koike, M., Takami, A. & Kondo, Y. (2016a). Hygroscopicity of materials internally mixed with black carbon measured in Tokyo. *Journal of Geophysical Research: Atmospheres*, *121*(1), pp.362-381.

Ohata, S., Moteki, N., Mori, T., Koike, M. & Kondo, Y. (2016b). A key process controlling the wet removal of aerosols: new observational evidence. *Scientific reports*, *6*, p.34113.

Oshima, N., Kondo, Y., Moteki, N., Takegawa, N., Koike, M., Kita, K., et al. (2012). Wet removal of black carbon in Asian outflow: Aerosol Radiative Forcing in East Asia (A-FORCE) aircraft campaign. *Journal of Geophysical Research: Atmospheres*, *117*(D3)

Perring, A.E., Schwarz, J.P., Gao, R.S., Heymsfield, A.J., Schmitt, C.G., Schnaiter, M. & Fahey, D.W. (2013). Evaluation of a perpendicular inlet for airborne sampling of interstitial submicron black-carbon aerosol. *Aerosol Science and Technology*, *47*(10), pp.1066-1072.

Peterson, D.A., Hyer, E.J., Campbell, J.R. & Xian, P. (2017, December). Meteorology Influencing Pollution Regimes and Transport during KORUS-AQ. In *AGU Fall Meeting Abstracts*.

Petzold, A., Ogren, J.A., Fiebig, M., Laj, P., Li, S.M., Baltensperger, U., et al. (2013). Recommendations for reporting" black carbon" measurements. *Atmospheric Chemistry and Physics*, *13*(16), pp.8365-8379.

Prinn, R., Cunnold, D., Rasmussen, R., Simmonds, P., Alyea, F., Crawford, A., et al. (1987). Atmospheric trends in methylchloroform and the global average for the hydroxyl radical. *Science*, *238*(4829), pp.945-950.

Rex, D.F. (1950). Blocking action in the middle troposphere and its effect upon regional climate. *Tellus*, *2*(4), pp.275-301.

Sachse, G.W., Hill, G.F., Wade, L.O. & Perry, M.G. (1987). Fast-response, high-precision carbon monoxide sensor using a tunable diode laser absorption technique. *Journal of Geophysical Research: Atmospheres*, *92*(D2), pp.2071-2081.

Sachse, G.W., Collins, J.E., Hill, G.F., Wade, L.O., Burney, L.G. & Ritter, J.A. (1991). Airborne tunable diode laser sensor for high-precision concentration and flux measurements of carbon monoxide and methane. In *Measurement of atmospheric gases* (Vol. 1433, pp. 157-167). International Society for Optics and Photonics.

Samset, B.H. & Myhre, G. (2011). Vertical dependence of black carbon, sulphate and biomass burning aerosol radiative forcing. *Geophysical Research Letters*, *38*(24).

Samset, B.H., Myhre, G., Schulz, M., Balkanski, Y., Bauer, S., Berntsen, T.K., et al. (2013). Black carbon vertical profiles strongly affect its radiative forcing uncertainty. *Atmospheric Chemistry and Physics*, *13*(5), pp.2423-2434.

Samset, B.H. & Myhre, G. (2015). Climate response to externally mixed black carbon as a function of altitude. *Journal of Geophysical Research: Atmospheres*, *120*(7), pp.2913-2927.

Schutgens, N.A., Gryspeerdt, E., Weigum, N., Tsyro, S., Goto, D., Schulz, M. & Stier, P. (2016). Will a perfect model agree with perfect observations? The impact of spatial sampling. *Atmospheric Chemistry and Physics*, *16*(10), pp.6335-6353.

Schwarz, J.P., Gao, R.S., Fahey, D.W., Thomson, D.S., Watts, L.A., Wilson, J.C., et al. (2006). Single-particle measurements of midlatitude black carbon and light-scattering aerosols from the boundary layer to the lower stratosphere. *Journal of Geophysical Research: Atmospheres*, *111*(D16).

Schwarz, J.P., Gao, R.S., Spackman, J.R., Watts, L.A., Thomson, D.S., Fahey, D.W., et al. (2008a). Measurement of the mixing state, mass, and optical size of individual black carbon particles in urban and biomass burning emissions. *Geophysical Research Letters*, *35*(13).

Schwarz, J.P., Spackman, J.R., Fahey, D.W., Gao, R.S., Lohmann, U., Stier, P., et al. (2008b). Coatings and their enhancement of black carbon light absorption in the tropical atmosphere. *Journal of Geophysical Research: Atmospheres*, *113*(D3).

Schwarz, J.P., Spackman, J.R., Gao, R.S., Watts, L.A., Stier, P., Schulz, M., et al. (2010a). Global-scale black carbon profiles observed in the remote atmosphere and compared to models. *Geophysical Research Letters*, *37*(18).

Schwarz, J.P., Spackman, J.R., Gao, R.S., Perring, A.E., Cross, E., Onasch, T.B., et al. (2010b). The detection efficiency of the single particle soot photometer. *Aerosol Science and Technology*, *44*(8), pp.612-628.

Schwarz, J.P., Gao, R.S., Perring, A.E., Spackman, J.R. & Fahey, D.W. (2013a). Black carbon aerosol size in snow. *Scientific reports*, *3*.

Schwarz, J.P., Samset, B.H., Perring, A.E., Spackman, J.R., Gao, R.S., Stier, P., et al. (2013b). Global-scale seasonally resolved black carbon vertical profiles over the Pacific. *Geophysical Research Letters*, *40*(20), pp.5542-5547.

Schwarz, J.P., Weinzierl, B., Samset, B.H., Dollner, M., Heimerl, K., Markovic, M.Z., et al. (2017). Aircraft measurements of black carbon vertical profiles show upper tropospheric variability and stability. *Geophysical Research Letters*, *44*(2), pp.1132-1140.

Shen, Z., Liu, J., Horowitz, L.W., Henze, D.K., Fan, S., Mauzerall, D.L., et al. (2014). Analysis of transpacific transport of black carbon during HIPPO-3: implications for black carbon aging. *Atmospheric Chemistry and Physics*, *14*(12), pp.6315-6327.

Shiraiwa, M., Kondo, Y., Moteki, N., Takegawa, N., Miyazaki, Y. & Blake, D.R. (2007). Evolution of mixing state of black carbon in polluted air from Tokyo. *Geophysical Research Letters*, *34*(16).

Shiraiwa, M., Kondo, Y., Moteki, N., Takegawa, N., Sahu, L.K., Takami, A., et al. (2008). Radiative impact of mixing state of black carbon aerosol in Asian outflow. *Journal of Geophysical Research: Atmospheres*, *113*(D24).

Slowik, J.G., Cross, E.S., Han, J.H., Davidovits, P., Onasch, T.B., Jayne, J.T., et al. (2007). An inter-comparison of instruments measuring black carbon content of soot particles. *Aerosol Science and Technology*, *41*(3), pp.295-314.

Simpson, I.J., Akagi, S.K., Barletta, B., Blake, N.J., Choi, Y., Diskin, G.S., et al. (2011). Boreal forest fire emissions in fresh Canadian smoke plumes: C 1-C 10 volatile organic compounds (VOCs), CO 2, CO, NO 2, NO, HCN and CH 3 CN. *Atmospheric Chemistry and Physics*, *11*(13), pp.6445-6463.

Spackman, J.R., Schwarz, J.P., Gao, R.S., Watts, L.A., Thomson, D.S., Fahey, D.W., et al. (2008). Empirical correlations between black carbon aerosol and carbon monoxide in the lower and middle troposphere. *Geophysical Research Letters*, *35*(19).

Stein, A.F., Draxler, R.R., Rolph, G.D., Stunder, B.J., Cohen, M.D. & Ngan, F. (2015). NOAA's HYSPLIT atmospheric transport and dispersion modeling system. *Bulletin of the American Meteorological Society*, *96*(12), pp.2059-2077.

Stephens, M., Turner, N. & Sandberg, J. (2003). Particle identification by laser-induced incandescence in a solid-state laser cavity. *Applied optics*, *42*(19), pp.3726-3736.

Stier, P., Seinfeld, J.H., Kinne, S., Feichter, J. & Boucher, O. (2006). Impact of nonabsorbing anthropogenic aerosols on clear-sky atmospheric absorption. *Journal of Geophysical Research: Atmospheres*, *111*(D18).

Stjern, C.W., Samset, B.H., Myhre, G., Forster, P.M., Hodnebrog, Ø., Andrews, T., et al. (2017). Rapid adjustments cause weak surface temperature response to increased black carbon concentrations. *Journal of Geophysical Research: Atmospheres*, *122*(21).

Ueda, S., Nakayama, T., Taketani, F., Adachi, K., Matsuki, A., Iwamoto, Y., et al. (2016). Light absorption and morphological properties of soot-containing aerosols observed at an East Asian outflow site, Noto Peninsula, Japan. *Atmospheric Chemistry and Physics*, *16*(4), pp.2525-2541.

Vollmer, M.K., Young, D., Trudinger, C.M., Mühle, J., Henne, S., Rigby, M., et al. (2018). Atmospheric histories and emissions of chlorofluorocarbons CFC-13 (CClF 3), ΣCFC-114 (C 2 Cl 2 F 4), and CFC-115 (C 2 ClF 5). *Atmospheric Chemistry and Physics*, *18*(2), pp.979-1002.

Wang, Q., Jacob, D.J., Spackman, J.R., Perring, A.E., Schwarz, J.P., Moteki, N., et al. (2014a). Global budget and radiative forcing of black carbon aerosol: Constraints from pole-to-pole (HIPPO) observations across the Pacific. *Journal of Geophysical Research: Atmospheres*, *119*(1), pp.195-206.

Wang, Q., Schwarz, J.P., Cao, J., Gao, R., Fahey, D.W., Hu, T., et al. (2014b). Black carbon aerosol characterization in a remote area of Qinghai–Tibetan Plateau, western China. *Science of the Total Environment*, *479*, pp.151-158.

Warneke, C., De Gouw, J. A., Goldan, P. D., Kuster, W. C., Williams, E. J., Lerner, B. M., et al. (2004). "Comparison of daytime and nighttime oxidation of biogenic and anthropogenic VOCs along the New England coast in summer during New England Air Quality Study 2002." *Journal of Geophysical Research: Atmospheres* 109, no. D10.

Warneke, C., De Gouw, J.A., Stohl, A., Cooper, O.R., Goldan, P.D., Kuster, W.C., et al. (2006). Biomass burning and anthropogenic sources of CO over New England in the summer 2004. *Journal of Geophysical Research: Atmospheres*, *111*(D23).

Wiedinmyer, C., Akagi, S.K., Yokelson, R.J., Emmons, L.K., Al-Saadi, J.A., Orlando, J.J. & Soja, A.J. (2011). The Fire INventory from NCAR (FINN): a high resolution global model to estimate the emissions from open burning. *Geoscientific Model Development*, *4*(3), p.625.

Wu, Y., Wang, X., Tao, J., Huang, R., Tian, P., Cao, J., et al. (2017). Size distribution and source of black carbon aerosol in urban Beijing during winter haze episodes. *Atmospheric Chemistry and Physics*, *17*(12), pp.7965-7975.

Yang, Y., Wang, H., Smith, S.J., Ma, P.L. & Rasch, P.J. (2017). Source attribution of black carbon and its direct radiative forcing in China. *Atmospheric Chemistry and Physics*, *17*(6), pp.4319-4336.

Zarzycki, C.M. & Bond, T.C. (2010). How much can the vertical distribution of black carbon affect its global direct radiative forcing?. *Geophysical Research Letters*, *37*(20).

Table 1. Regional contributions to black carbon direct radiative effect over South Korea, determined from integrating the observed rBC mass burden in South Korea with the regional normalized direct radiative effect. The top four rows give the regional DRE contributions for each meteorological period, and the bottom row is for the entire campaign. Estimated variability was calculated from the range of DRE for each vertical profile included in the analysis based on the BC mass variability. The relative contributions by region were based upon the contributions to the average profile for each period, for observations between 1000 and 400 hPa. The high-altitude contribution was based on the percent of the total DRE for that period; the upper limit (assuming constant BC mass mixing ratio between 400 hPa and 200 hPa) is shown in parentheses. As discussed in Section 2.2, the estimated contributions for South Korea given in the table provide only an upper bound on local influence.

Meteorological Period/ Campaign	**Average Regional DRE (W/m^2)**	**South Korea**	**North Korea**	**Marine & Japan**	**China**	**Mongolia**	**Russia**	**Central Asia**	**Long Range Transport**	**High altitude (>400 hPa)**
Dynamic	$0.9^{+0.6}_{-0.4}$	28%	0%	6%	22%	2%	14%	5%	10%	14% (24%)
Stagnant	$0.7^{+0.2}_{-0.2}$	32%	0%	21%	24%	2%	4%	3%	0.5%	13% (15%)
Extreme Pollution*	$1.5^{+0.5}_{-0.8}$	*34*%	0%	1%	*29*%	3%	16%	7%	4%	7% (9%)
Rex Blocking	$0.9^{+0.3}_{-0.4}$	27%	14%	5%	23%	1%	17%	2%	0.1%	11% (16%)
KORUS-AQ	$\mathbf{1.0^{+0.9}_{-0.5}}$	**31%**	**2%**	**8%**	**22%**	**2%**	**14%**	**5%**	**3%**	**12% (19%)**

*Higher boundary layer values than the other 3 meteorological periods indicated likely influence from Chinese pollution at the surface. See discussion in Section 5.2.

Figure 1. NASA DC-8 flight tracks during KORUS-AQ, color-coded by the BC mass mixing ratio in the boundary layer for 60 s averaged SP2 observations. KORUS-AQ flight tracks for all 20 research flights are shown in blue. Highest boundary layer values of BC were measured in the SMA, and during flights targeting periods of significant Chinese outflow over the Yellow Sea. Repeated measurements over the SMA (box and inset) provided vertical sampling of BC in the same location over the course of the campaign. The spirals over Taehwa Research Forest were located at approximately 37.4°N and 127.6°E, approximately 30 km southeast of Seoul.

Figure 2. Last boundary layer position for air parcels observed during vertical sampling over the Taehwa Research Forest derived from the Hysplit 5-day back trajectory analysis for each minute of flight data. The size indicates the average rBC mass loading measured during that minute (larger size indicates higher observed mass), and color indicates the pressure altitude at which that air parcel was observed. Regions used in the source-attribution analysis are shown.

Figure 3. BC tracer-tracer relationships by source region. Both rBC mass and average coating thickness for 4-6 fg rBC cores (shown as 60 s averages, with coating thickness indicated by color scale) associated with different source regions indicate correlation with CO (characteristic of different combustion sources), CH_3CN (indicative of biomass burning/coal combustion), and CH_2Cl_2 (indicative of industrial sources). Distinct tracer-tracer relationships were observed for different regions; filled circles indicate source attribution from last interaction with the boundary layer and open circles from longest residence time (discussed in Section 2.2). The black line shows the best linear fit

for the tracer-tracer relationship for that region, with the red dashed line showing the best linear fit for South Korea. The value for the slope and its 95% confidence interval for the fit parameter are shown for each tracer-tracer relationship, as well as the R^2 value. L.R.T. is long range transport.

Figure 4. Observed black carbon mass mixing ratio (a), coating thickness (b), rBC mass median diameter (c), and BC/CO slope (d) by meteorological period. Vertical profiles of rBC mass loadings, average coatings for 4-6 fg rBC cores, mass median diameter, and BC/CO slopes during sampling over Taehwa Research Forest demonstrated variability at all observed altitudes. Vertical profiles from each spiral are shown as lighter dashed lines, color-coded by their meteorological period (those not associated with a meteorological period are black). Average vertical profiles for each meteorological period are shown as bolded, thicker lines and markers. For the rBC mass median diameter, individual profiles are shown as dashed lines, with the size of the marker (hollow circle) indicating the number of rBC particles measured in that layer. For the BC/CO slope, the size of the marker indicates the correlation coefficient between BC and CO for that bin, with larger sizes indicating stronger correlation.

Figure 5. Regional contributions to vertically resolved black carbon concentrations for each meteorological period. Relative contributions of source regions to BC mass loadings by altitude were determined from the observations and the Hysplit back trajectory analysis for each meteorological period. The back trajectories demonstrate significant fluctuations in source region over a relatively short time scale due to synoptic-scale meteorology. The boundary layer contributions provided an upper limit on local influence; see discussion in Section 4.2. Horizontal light blue lines show the average (solid) and minimum and maximum (dashed) height of the boundary layer during each meteorological period.

Figure 6. Regional contributions to vertically resolved black carbon observations. Left: Average campaign vertical profile of rBC mass burden (solid black line and markers) and vertical dependence of normalized direct radiative forcing (dashed black line) for observations over a rural site SE of Seoul (Taehwa Research Forest). Error bars indicate 1 standard deviation (assuming measurements in each bin are Gaussian distributed and therefore are only shown for the higher range on the log plot). Right: Relative contributions of source regions during KORUS-AQ along with the BC radiative effect by height for each altitude bin (dashed-dotted black line), indicate where contributions are most important for the total column direct radiative effect. Horizontal light blue lines show the average (solid) and minimum and maximum (dashed) height of the boundary layer during the campaign.

Figure 7. Comparison of KORUS-AQ measurements to A-FORCE campaigns. Left: The spatial distribution of vertical sampling periods is shown at their average latitude and longitude locations for KORUS-AQ, A-FORCE 2009, and A-FORCE 2013W. Right: Average rBC mass burden observed over the Yellow Sea (right) during the spring/summer 2016 KORUS-AQ campaign (bolded red line and markers) was cleaner at higher altitudes than observations during the A-FORCE 2009 campaign (spring 2009, bolded green lines and markers) and similar to A-FORCE W2013 (winter 2013, bolded blue lines and markers). The seasonally resolved regional NDRF over the Yellow Sea is also shown (dashed lines, color-coded by season).

Figure 1.

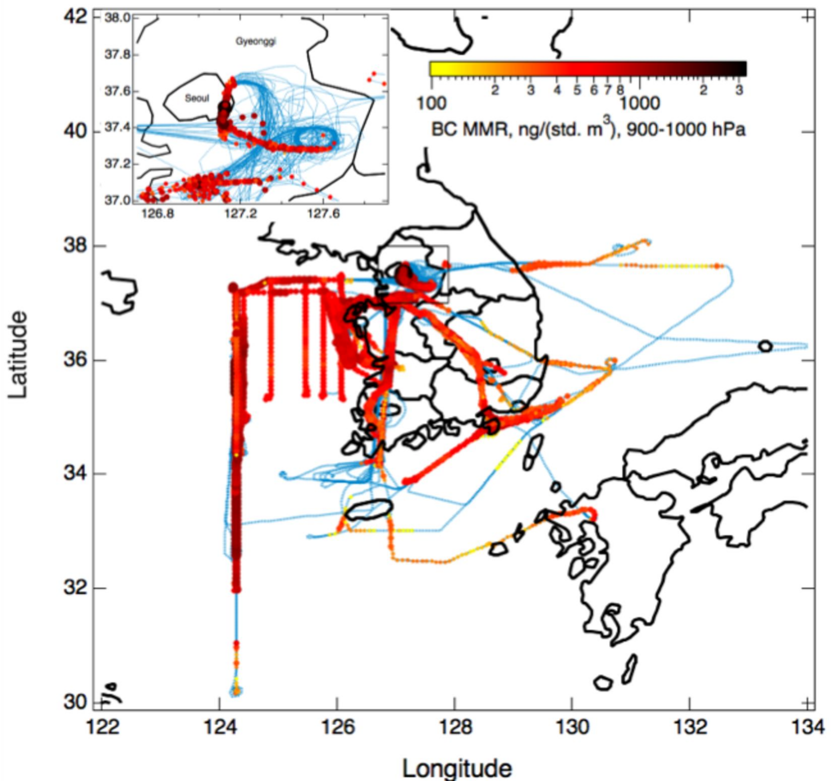

Gyeonggi
Seoul
38.0
37.8
37.6
37.4
37.2
37.0
126.8
127.2
127.6
100
2
3
4
5
6
7
8
1000
2
3
BC MMR, ng/(std. m^3), 900-1000 hPa
42
40
38
36
34
32
30
Latitude
122
124
126
128
130
132
134
Longitude

Figure 2.

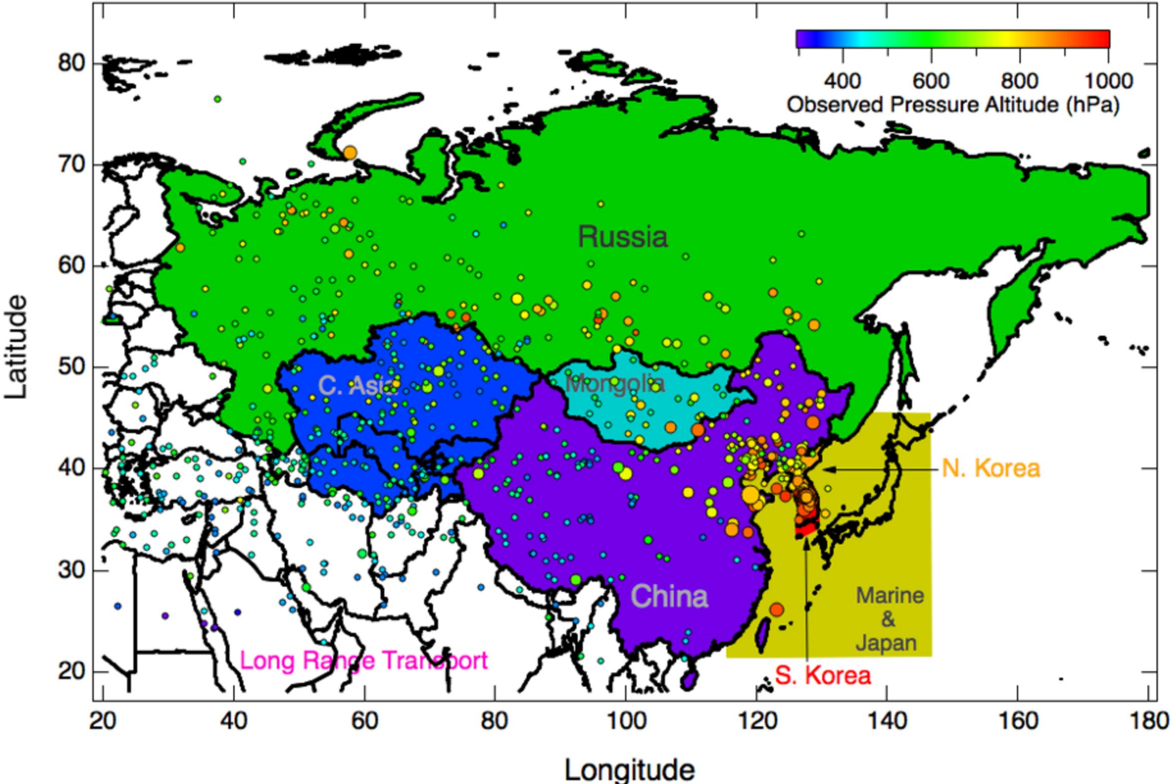

400
600
800
1000
Observed Pressure Altitude (hPa)
Russia
C. Asia
Mongolia
China
N. Korea
S. Korea
Marine & Japan
Long Range Transport
Latitude
Longitude
80
70
60
50
40
30
20
20
40
60
80
100
120
140
160
180

Figure 3.

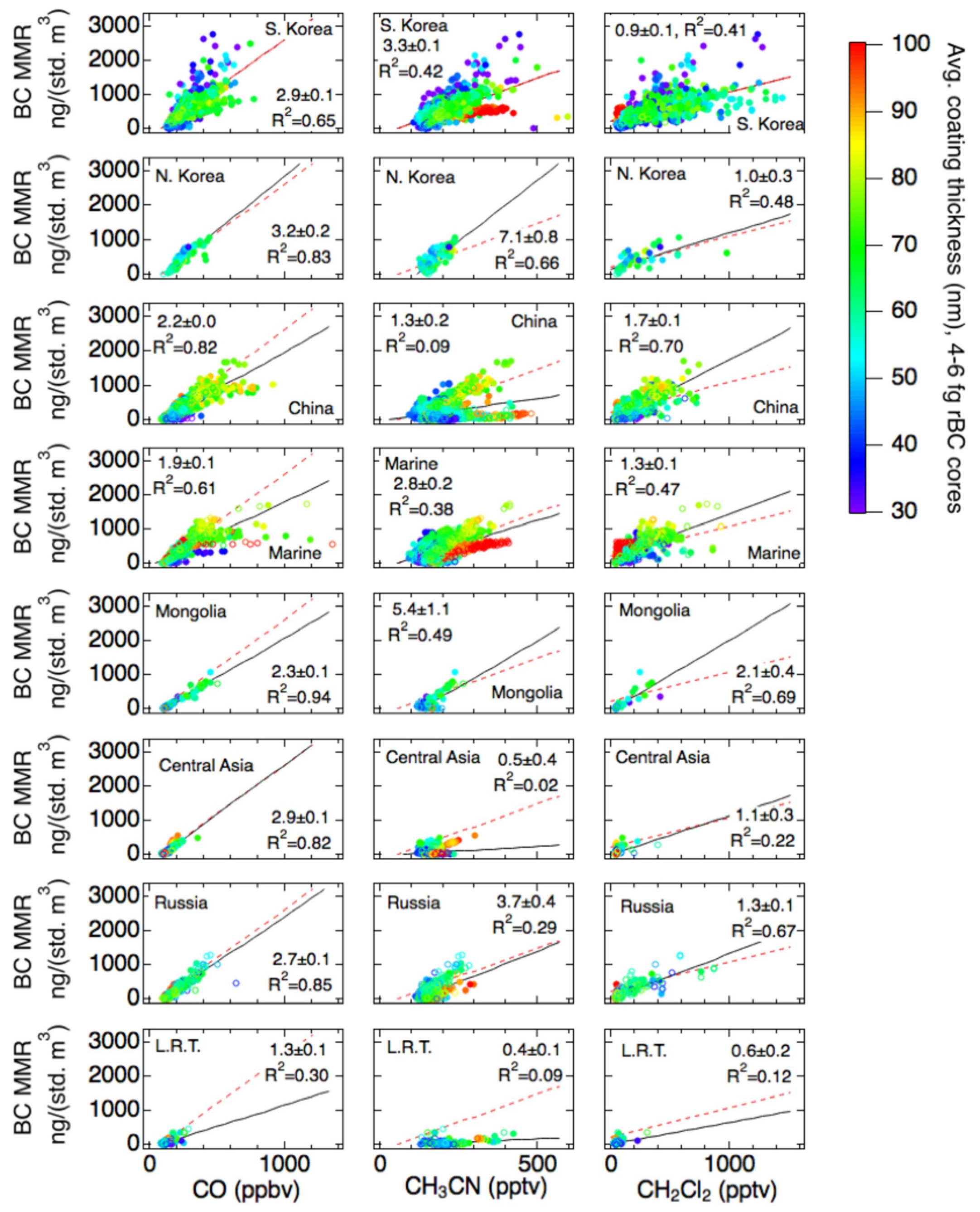

BC MMR ng/(std. m3)
S. Korea
2.9±0.1
R2=0.65
S. Korea
3.3±0.1
R2=0.42
0.9±0.1, R2=0.41
S. Korea
N. Korea
3.2±0.2
R2=0.83
N. Korea
7.1±0.8
R2=0.66
N. Korea
1.0±0.3
R2=0.48
2.2±0.0
R2=0.82
China
1.3±0.2
R2=0.09
China
1.7±0.1
R2=0.70
China
1.9±0.1
R2=0.61
Marine
Marine
2.8±0.2
R2=0.38
1.3±0.1
R2=0.47
Marine
Mongolia
2.3±0.1
R2=0.94
5.4±1.1
R2=0.49
Mongolia
Mongolia
2.1±0.4
R2=0.69
Central Asia
2.9±0.1
R2=0.82
Central Asia
0.5±0.4
R2=0.02
Central Asia
1.1±0.3
R2=0.22
Russia
2.7±0.1
R2=0.85
Russia
3.7±0.4
R2=0.29
Russia
1.3±0.1
R2=0.67
L.R.T.
1.3±0.1
R2=0.30
L.R.T.
0.4±0.1
R2=0.09
L.R.T.
0.6±0.2
R2=0.12
CO (ppbv)
CH3CN (pptv)
CH2Cl2 (pptv)
Avg. coating thickness (nm), 4-6 fg rBC cores

Figure 4.

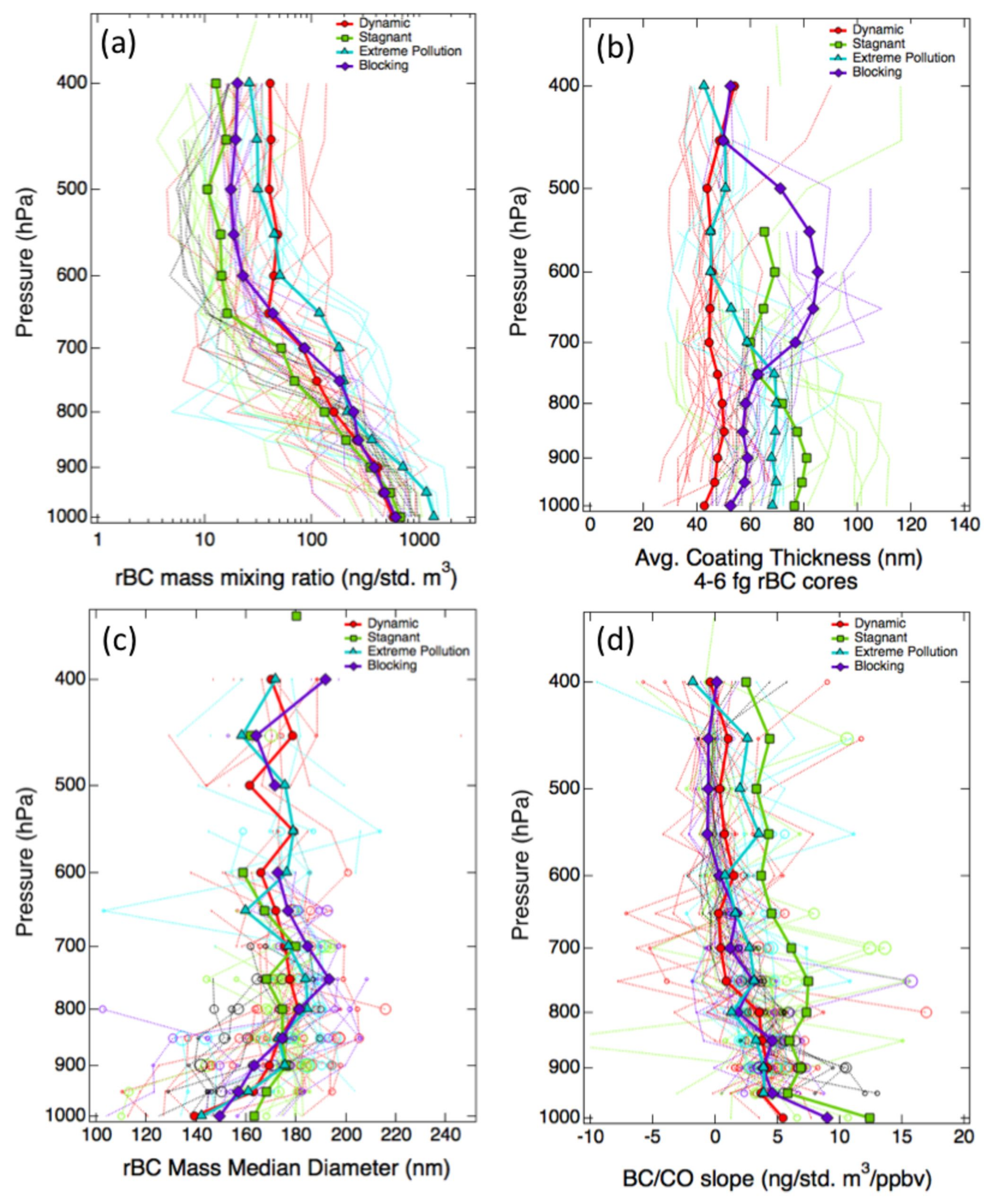
(a)
Dynamic
Stagnant
Extreme Pollution
Blocking
Pressure (hPa)
rBC mass mixing ratio (ng/std. m³)
(b)
Avg. Coating Thickness (nm)
4-6 fg rBC cores
(c)
rBC Mass Median Diameter (nm)
(d)
BC/CO slope (ng/std. m³/ppbv)

Figure 5.

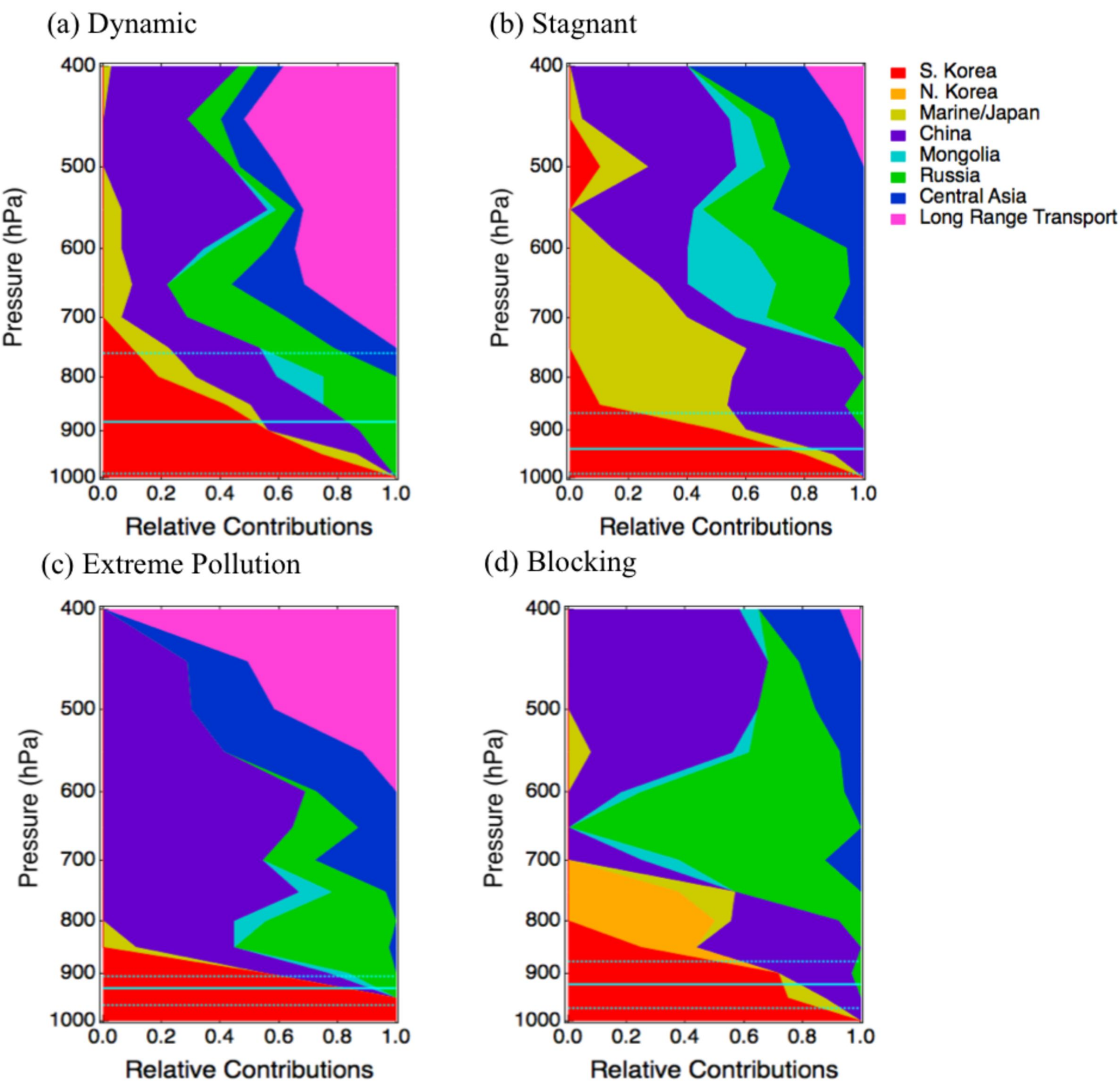
(a) Dynamic
(b) Stagnant
(c) Extreme Pollution
(d) Blocking
Pressure (hPa)
400
500
600
700
800
900
1000
0.0
0.2
0.4
0.6
0.8
1.0
Relative Contributions
S. Korea
N. Korea
Marine/Japan
China
Mongolia
Russia
Central Asia
Long Range Transport

Figure 6.

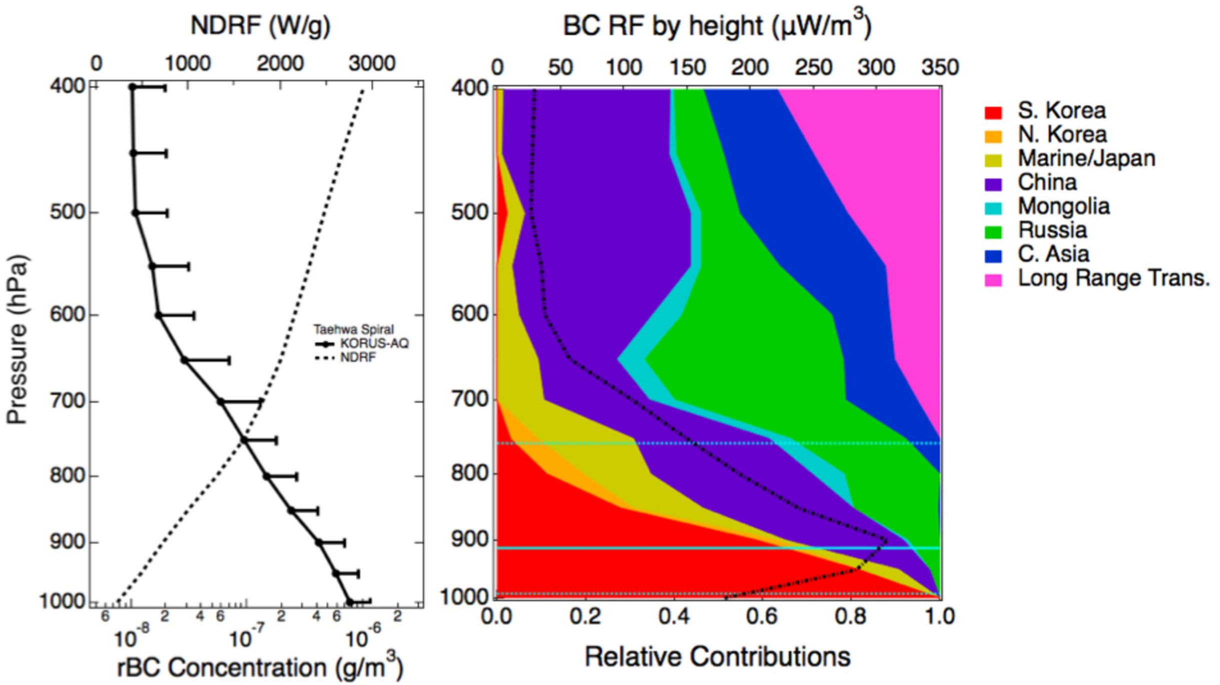

NDRF (W/g)
0
1000
2000
3000
400
500
600
700
800
900
1000
Pressure (hPa)
Taehwa Spiral
KORUS-AQ
NDRF
6
2
4
6
2
4
6
2
10^{-8}
10^{-7}
10^{-6}
rBC Concentration (g/m^3)
BC RF by height (µW/m^3)
0
50
100
150
200
250
300
350
0.0
0.2
0.4
0.6
0.8
1.0
Relative Contributions
S. Korea
N. Korea
Marine/Japan
China
Mongolia
Russia
C. Asia
Long Range Trans.

Figure 7.

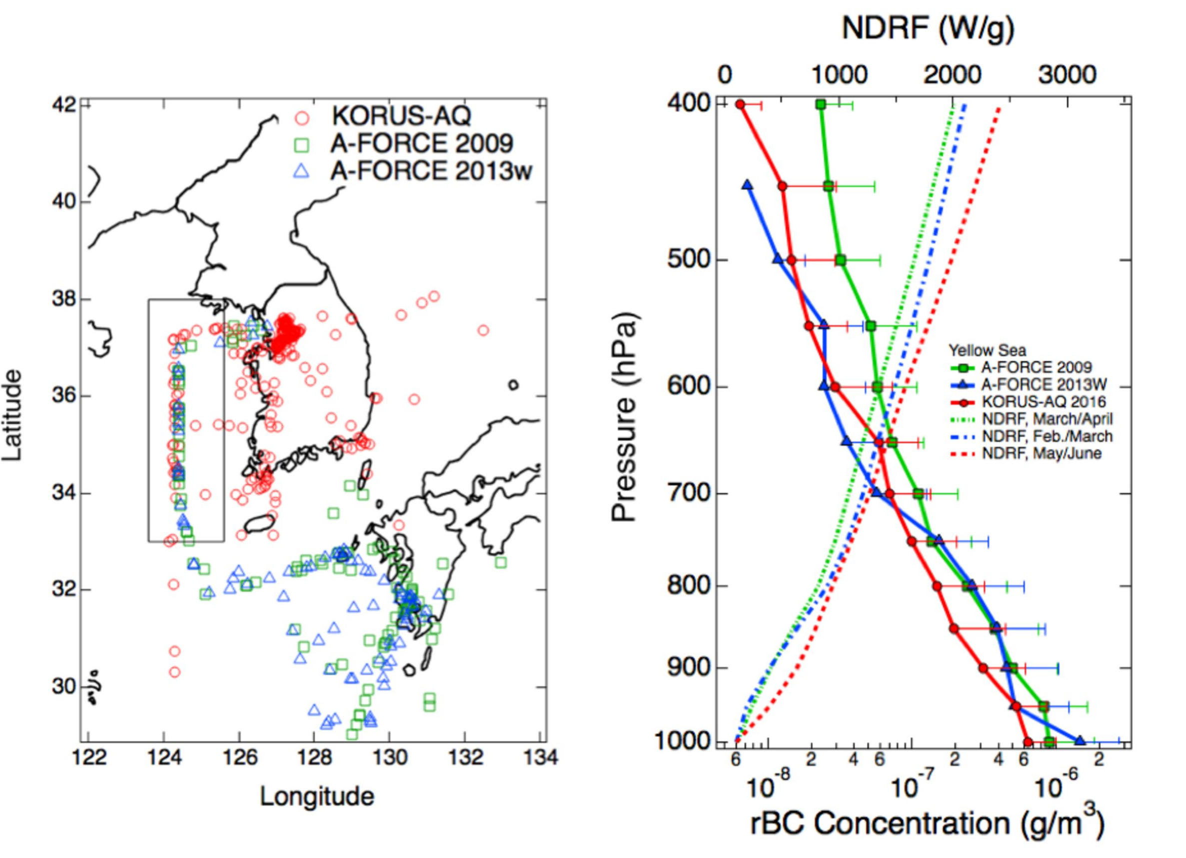

KORUS-AQ
A-FORCE 2009
A-FORCE 2013w
Latitude
Longitude
NDRF (W/g)
Pressure (hPa)
Yellow Sea
A-FORCE 2009
A-FORCE 2013W
KORUS-AQ 2016
NDRF, March/April
NDRF, Feb./March
NDRF, May/June
rBC Concentration (g/m^3)